

Fig. 8. Gas evolution model

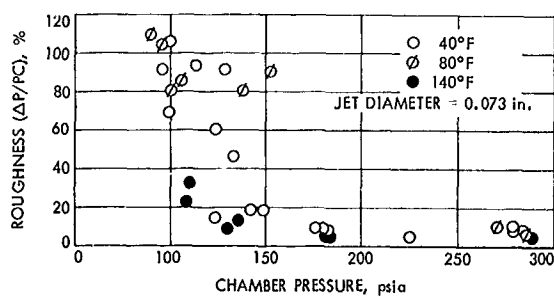


Fig. 9. Roughness with a single unlike doublet

fluctuations (ΔP) up to 100% as a function of average chamber pressures (PC) and propellant temperature. The frequency ranged from 100–250 Hz.

4. Conclusions

The experimental data shows that combustion effects can produce mixture ratio distributions that are significantly different from those obtained in simulated cold-flow tests. When using such cold-flow data, the stream separation criteria should be checked to establish that the element will operate in a non-separated region. This probably applies not only to mixture ratio distributions, but also to mass and drop-size distributions.

Reference

1. Kushida, R., and Houseman, J., *Criteria for Separation of Impinging Streams of Hypergolic Propellants*, Technical Memorandum 33-395. Jet Propulsion Laboratory, Pasadena, Calif., July 15, 1968.

N 69 138

XV. Lunar and Planetary Instruments

SPACE SCIENCES DIVISION

A. A Mars Meteorology Wind Tunnel, J. M. Conley

1. Introduction

This article is based on the assumption that it will be desirable for the first Mars lander to be capable of measuring the atmospheric temperatures and wind velocities of Mars. Trade-off studies for the selection of specific instruments for wind measurement have been inconclusive (SPS 37-53, Volume III, pp. 136-143) and more detailed data on the operation of various instrument types under the Mars surface environment are required in order to thoroughly evaluate the instruments for this application. Experimental determination of the heat transfer parameters of immersion thermometers under simulated Mars surface conditions is also necessary. It would, of course, be desirable to simulate all of the relevant environmental parameters, which may include, depending on the instrument under test, gas composition, pressure, and temperature; wind speed; solar radiation; surface temperature; atmospheric dust and gravity. However, if the candidate instruments can be tested under conditions approximating those at the Mars surface, then scaling procedures will allow close estimates of their performance for any given Mars model atmosphere. It does *not* follow that the performance of the various instruments under

earth-surface atmospheric conditions can be readily scaled to the Mars conditions since the density ratio of the two atmospheres is of the order of 100 and small errors in the measurements would result in considerable errors when extrapolated to the Mars conditions. Furthermore, scaling procedures applied over this large density ratio would require extremely delicate measurements of forces, temperatures differences, etc., and would not be nearly as convincing as actual operation of the instruments under simulated Mars conditions.

A small wind tunnel capable of simulating the expected Mars surface pressures and wind speed has been built and is described in this article. Original design goals for the tunnel included test section speeds in the range of 0-466 ft/s at gas densities of 10^{-5} - 4×10^{-5} g/cm³ corresponding to Mars surface pressures of 5-20 mbars.

2. Design Studies

a. Basic options. It was required that the system allow simulation of the critical environmental parameters for the aforementioned instrument types. For the anemometers, if both Reynolds numbers and speed are simulated, only small corrections to the data would be required for

the other parameters of interest. In later phases, it may be desirable to include atmospheric dust and temperature, but, in many cases, these can be simulated independently of Reynolds number and speed, i.e., with other facilities. For the immersion thermometer work, it would also be desirable to simulate thermal radiation and gas temperature environment. The solar thermal radiation incident on a small sensor can be simulated with a small light source and the infrared radiation by shrouds surrounding the sensor. Gas temperature control can be accomplished by means of a heat exchanger upstream of the sensor. Although these features were not incorporated into the design, they can be added at a later date.

Ideally, the test section would be a black-body, anechoic chamber with linear dimensions of about 10 ft. This would allow testing of sonic anemometer arrays and other large instruments. Such a system is not within the scope of the present program. A rotating arm within a vacuum system was considered but rejected because of the relatively large forces that would arise due to rotation. Thus, a wind tunnel is required.

A minimum test section size of about 1-ft² cross section is determined by the rotating-cup anemometer, which has a projected area of about 4 in.². Thus, a volume flow rate of 460 ft³/s (27,000 ft³/min) is desirable. Two pumping techniques were considered: (1) ejector pumps exhausting to the atmosphere, and (2) a recirculating fan operating within a vacuum system. At the maximum anticipated test section pressure, a throughput of about 5×10^5 torr-liter/s would be required. Since a very large, costly high maintenance steam ejection facility would be necessary, this technique was rejected.

No information was available on the performance of commercial fans at the densities of interest. Measurements of the head of a small aircraft fan blade at blade Reynolds numbers approximating those of a larger commercial fan (both of vaned axial construction) indicated that good performance could be obtained down to pressures of approximately 5 mbars of air at a standard temperature, corresponding to the lowest expected Mars surface pressures and fan blade Reynolds numbers. A surplus jet engine compressor might also have been used. Such fans, which operate with supersonic blade tip speeds, are capable of producing a relative total head $\Delta p/p$ of approximately 0.5 per stage, where Δp is the total head and p is the inlet static pressure. In contrast, the commercial fan selected yields only $\Delta p/p = 0.022$ per stage. However, it was inexpensive, readily available, required no expensive modification, and was deemed adequate for the application.

b. Tunnel loop losses. An existing vacuum system and a tank 4 ft in diameter by 16 ft long was available. Even though the disadvantages of an annular construction were realized (Ref. 1), it was the most economical means of achieving the desired test section conditions. Head losses to be considered in the design included those due to skin friction, screens, corners, and diffuser inefficiency.

The desired maximum test section speed of 460 ft/s requires a fan $\Delta p/p = 0.12$, independent of gas density. Loop losses would add to this requirement and any head recovery in the diffuser would lessen it. However, the available vacuum tank allowed space for only a two-stage fan with a $\Delta p/p = 0.044$. Thus, a maximum speed of 280 ft/s could be achieved assuming no friction losses and zero diffuser efficiency. A friction loss of 15% of total head would result in a maximum speed of approximately 265 ft/s. Although this falls far short of the original 460 ft/s design goal, it was considered to be adequate for critical tests required to evaluate the performance of the instruments in question. Higher Reynolds numbers and dynamic pressures can be achieved by operating at higher pressures.

Since turbulence levels of the order of several percent could be tolerated, neither turning vanes nor screens were incorporated into the initial design. However, provisions were made for adding them at a later date if they proved to be necessary.

The diffuser efficiency to be expected was unknown, although criteria established for higher Reynolds numbers than those occurring in the diffuser indicated that boundary layer separation would occur and that diffuser efficiency would be quite low. For design purposes, it was assumed to be zero and any actual head recovery in the diffuser would allow re-setting of the fan-blade pitch to increase the maximum test section speed attainable. The only appreciable skin friction losses occur at and near the test section and were calculated to be approximately 10% of the fan head. Lack of a diffuser at the fan exit would also result in some loss of head. In the absence of screens, the loss around the loop should not exceed 15% of the fan head, excluding that due to diffuser inefficiency.

3. Final Design

Figure 1 is a cross-sectional view of the system, approximately to scale, and Figure 2 is a photograph of the nozzle and test section taken through the 5-ft diam vacuum tank port.

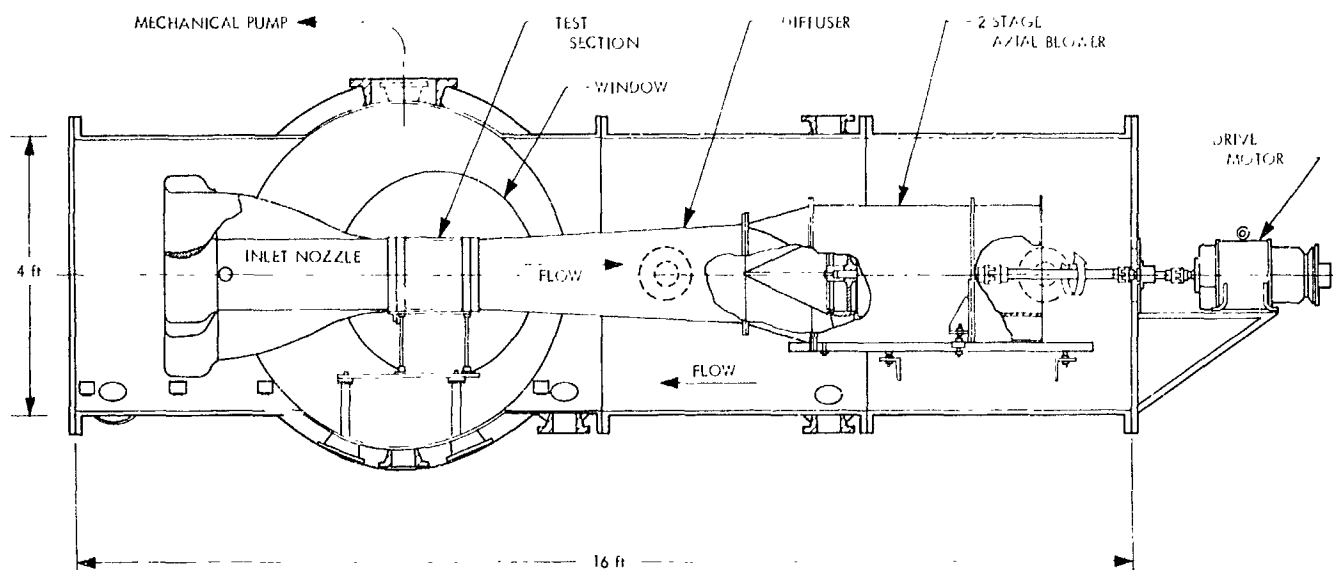


Fig. 1. Mars wind tunnel cross section



Fig. 2. Nozzle and test section

The nozzle entrance is hexagonal in shape. Four of the eight sides taper to zero width at the test section such that, in cross section, the sides appear as two cubic curves of the form $y = ax^3/3$ on the entrance end of the nozzle and $y' = ax'^3$ on the exit end. The alternate sides are of constant 12-in. width. Nozzle length is 36 in. and the curves intersect, with equal slope, at a point 22.8 in. from the entrance. A nozzle entrance bell of 1.5-in. radius is provided. The area of the nozzle entrance was selected to provide approximately equal conductances in the nozzle entrance and in the annulus surrounding it. The contraction ratio is 4.8.

The test section is a 1-ft cube. Plexiglas windows, 8-in. diam, are provided on one side and the top, and a hinged plexiglas door 9-in. wide by 12-in. high forms the other side. A removable bottom plate can be readily replaced for various model configurations. No traverse mechanism has been provided, although it would be highly desirable since the system now must be vented in order to move a model or probe. Pumpdown time from one atmosphere to 10 mbars is approximately 3 min with the existing 300 ft³/min mechanical pump. On the basis of the data given in Ref. 2, the test section profile should be reasonably flat for speeds down to approximately 1 ft/s.

The diffuser half-angle is 3 deg and it is coupled to the fan by a transition section 1-ft long.

The fan is a two-stage, vaned axial 23.25-in. diam blower with a 14-in. hub. It is nominally rated at 50 hp, 3450 rev/min, 12,000 ft³/min at 18 in. of water Δp . Variable-pitch blades allow some latitude in the fan characteristics.

The direct drive motor is a silicon-controlled rectifier controlled variable speed dc motor with tachometer feedback. Although only 1 hp is required to drive the tunnel at the highest expected Mars atmosphere surface density, the high moment of inertia of the fan would result in a 10-min acceleration time to full speed and a similar deceleration time. For this reason, and also to allow operation at high Reynolds numbers, a 5-hp drive motor was chosen. Under constant load, its speed is stable at $\pm 1\%$ of set speed.

from 20-3500 rev/min. The motor is coupled through the vacuum tank end plate by an oil-lubricated, graphite-to-ceramic, rotating seal.

4. System Performance

The maximum test section speed achieved at 3450 rev/min, as measured by means of a pitot was found to be 240 ft/s at an air density of 2×10^{-5} g/cm³. Adjustment of the fan blade pitch should increase this to approximately 280 ft/s. Since this is in nearly exact agreement with the result of applying Bernoulli's equation to the characteristics published by the fan manufacturer, it must be assumed either that the diffuser head recovery balances the friction loss or that both are negligible. However, these are preliminary data and further measurements will be required since the fan inlet density is not known. The instrumentation necessary for more precise measurements is now being installed and more detailed performance information, including profiles and turbulence data, will be available in the near future.

The leak rate of the vacuum system results in a pressure increase of approximately 0.015 mbars/hr. This is much less than the rates associated with temperature changes due to venting and pumping down the system. It is not known how much of this leak rate is due to the rotating seal, but, since the total leak rate is negligible, the seal must be considered to be satisfactory. No seal wear has been detected after approximately 16 hr of operation.

The system can be operated easily by one man and should require very little maintenance. Although measurements of the test section speed profiles would be facilitated by a traverse system, the effort required to design and build one would not be justified at this time.

References

1. Pankhust, R. C., and Holder, D. W., *Wind Tunnel Technique*, Sir Isaac Pitman and Sons, Ltd., London, 1952.
2. Prandtl, L., and Tietjens, O. G., *Applied Hydro- and Aeromechanics*, Dover Publications, Inc., New York, N. Y., 1957.

XVI. Space Instruments

SPACE SCIENCES DIVISION

A. A Low-Noise Charge-Sensitive Video Preamplifier for Use With the SEC Camera Tube, D. F. Stout

1. Introduction

Handling of slow scan video information from the secondary electron conduction (SEC) camera tube requires an extension of techniques used with slow scan vidicons. At standard scanning rates (30 frames/s) the signal current from the target of an SEC camera tube has a signal-to-noise ratio of only 50 to 100. At slow scan speeds, similar to those used on *Mariner* television systems, the signal-to-noise ratio from the SEC camera tube is severely degraded. Work has been performed to overcome this drawback to a potentially useful spacecraft imaging camera tube.

2. Approach

The first consideration was to develop a television system that would effectively scan the SEC camera tube at high speeds and, at the same time, possess line and frame times which would be compatible with the space-

craft data handling capability. Two approaches to achieve the above result are being explored.

- (1) *Beam chopping.* This method allows the read beam to be on for only a short portion of the time it is scanning across each picture element (pixel). This generates pulses with amplitudes proportional to the quantity of charge stored on each pixel.
- (2) *Beam position modulation.* This technique utilizes a small fast vertical beam movement during the time the beam is slowly sweeping horizontally over each pixel. Again, this produces pulses of video information during the short vertical movement of the beam.

Either method results in fast low-noise pulses of video information. For a 1000×1000 -pixel raster, these pulses contain from approximately 10^{-16} to 10^{-14} C/pulse. An optimum method of preamplification was needed, so that the signal-to-noise ratio of this information would not be degraded. An extensive survey of various methods of low-noise preamplification was made prior to designing a charge-sensitive amplifier.

3. Preamplifier Design

Accuracy in charge measurements is enhanced by making these measurements independent of variations in source capacitance, amplifier input capacitance, and stray wiring capacitance. This is accomplished by making the effective amplifier input capacitance very large and also dependent only on passive temperature stable components.

The standard configuration (Fig. 1a) for such a device is a high-gain, high-quality, wide-bandwidth operational amplifier with a feedback network whose prime elements are a parallel capacitance C_f and resistor R_f .

The output of the circuit shown in Fig. 1a for an input charge impulse of magnitude Q is

$$e_2(t) = \frac{Q \exp[-t/(R_f C_f)]}{C_f}$$

The capacitor C_f should be as small as possible so that e_2 is sufficiently above noise before going to the next amplifier.

The capacitor C_f can be treated as if it were a Miller capacitance $C_f(1-A)$. If gain A approaches infinity, then

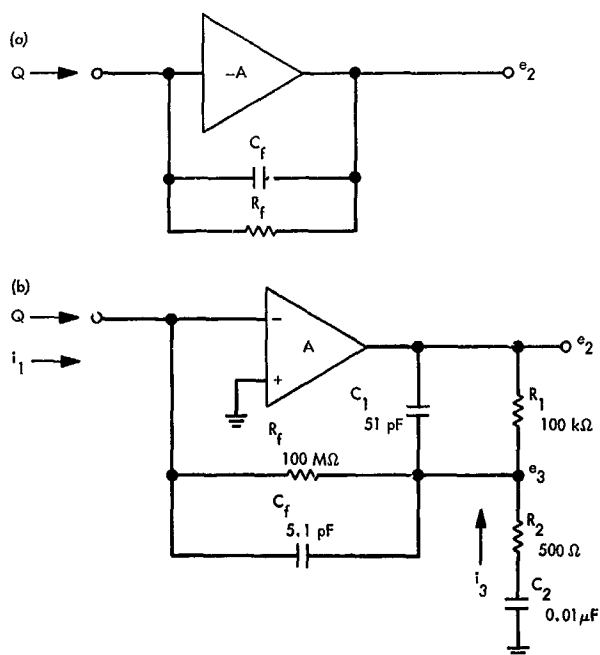


Fig. 1. Charge-sensitive amplifiers: (a) basic, (b) modified

essentially all incoming charge is deposited on C_f . The input impedance is therefore nearly zero for the charge pulse. For these reasons the device is called a charge-sensitive amplifier.

For the SEC camera tube, C_f must be only 0.1 pF if e_2 is to remain greater than 1 mV for all expected charge pulses. This would make C_f very difficult to realize with the required accuracy and stability. It would be better if C_f could be at least several picofarads.

If a 100:1 attenuator is placed between e_2 and the feedback network impedance Z_f , then several significant changes are made to the feedback circuit requirements: (1) R_f must be lowered in resistance 100 times, and (2) C_f must be raised in capacitance by 100 times. These changes will make the charge-to-voltage conversion gain identical with that of the original preamplifier. The new circuit diagram is shown in Fig. 1b.

Thus, C_f looks like $5.1 \text{ pF}/100 = 0.051 \text{ pF}$ as far as the conversion gain is concerned. Conversely, to the input, C_f appears to be $A_L C_f = 0.56 \text{ μF}$, where A_L = loop gain $= 0.01 A = 1.1 \times 10^5$. It is obvious that stray capacitance is negligible compared to 0.56 μF and should therefore have little effect on the conversion gain.

4. Attenuator Design

The attenuator requires careful design since it performs the pulse shaping for the entire preamplifier. This attenuator is sometimes referred to as a lead-lag network because over a given frequency range the phase shift is approximately zero. In the time domain, the parameters of the attenuator are chosen such that the rise and fall times are both 5 μs.

Some basic assumptions regarding the total television system must first be made before the attenuator design can be determined.

- (1) The picture format dimensions are chosen to be 1000×1000 pixels.
- (2) The sweep speed is 50 ms for the active portion of each line. This means the beam will reside over each pixel for 50 μs.
- (3) The duty cycle for beam chopping or beam position modulation is 2% so that the charge pulses have a width of 1 μs.

These assumptions are used to determine the preamplifier pulse shaping. With 49 μs between pixels, adequate time is available to form a good quality gaussian

pulse with rise and fall times of several microseconds. A gaussian pulse shape has very good characteristics upon which to perform an accurate analog-to-digital conversion. The pulse shape and time constants chosen are adequate to assure that the baseline will be within 1% of zero before the next pulse occurs.

The transfer function of the attenuator is

$$\begin{aligned}\frac{E_3(s)}{E_2(s)} &= \frac{(1 + T_1s)(1 + T_2s)}{T_1T_2s^2 + (T_1 + T_2 + T_{12})s + 1} \\ &= \frac{(1 + T_1s)(1 + T_2s)}{(1 + T_3s)(1 + T_4s)}\end{aligned}$$

where

$$T_1 = R_1C_1 = 5 \times 10^{-6} \text{ s} = \text{pulse rise time}$$

$$T_2 = R_2C_2 = 5 \times 10^{-6} \text{ s} = \text{pulse fall time}$$

$$T_{12} = R_1C_2$$

The magnitude of the attenuation is

$$\left| \frac{e_3}{e_2} \right| = \frac{T_1 + T_2}{T_1 + T_2 + T_{12}} = 0.01$$

Rearranging,

$$T_{12} = \frac{T_1 + T_2}{\left| \frac{e_3}{e_2} \right|} - T_1 - T_2 = 9.9 \times 10^{-4}$$

For physical size considerations, C_2 is first chosen to be $0.01 \mu\text{F}$. The other components then become as shown in Fig. 1b.

A Bode plot of the attenuator transfer function is shown in Fig. 2. Also shown on the same figure is the response as predicted by the CIRCS computer-aided circuit-analysis program. Figure 3 shows the phase plot as obtained with the CIRCS program, which is executed on the IBM 1620 computer.

5. Preamplifier Analysis With Attenuator Included

By assuming the operational amplifier has infinite gain, infinite input impedance, and zero output impedance, the analysis is greatly simplified. From Fig. 1b and the above three assumptions, the following equations are derived:

$$E_3 = I_1 Z_f = I_3 Z_2$$

or

$$I_1 = \frac{I_3 Z_2}{Z_f}$$

and

$$E_2 = I_3 (Z_1 + Z_2)$$

The transimpedance becomes

$$\frac{E_2}{I_1} = \frac{I_3(Z_1 + Z_2)}{I_3 Z_2 / Z_f} = \frac{Z_f(Z_1 + Z_2)}{Z_2} \quad (1)$$

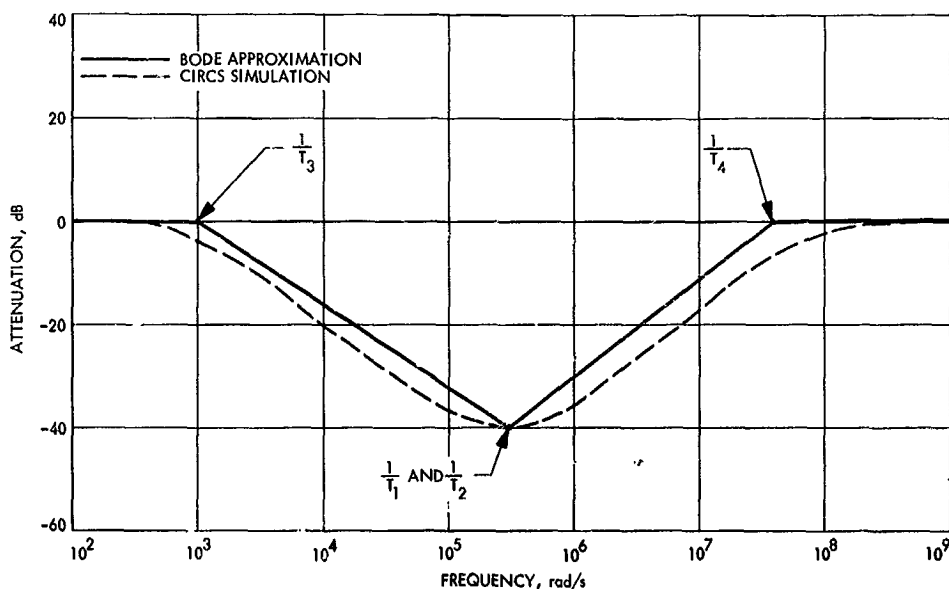


Fig. 2. Attenuation of lead-lag network

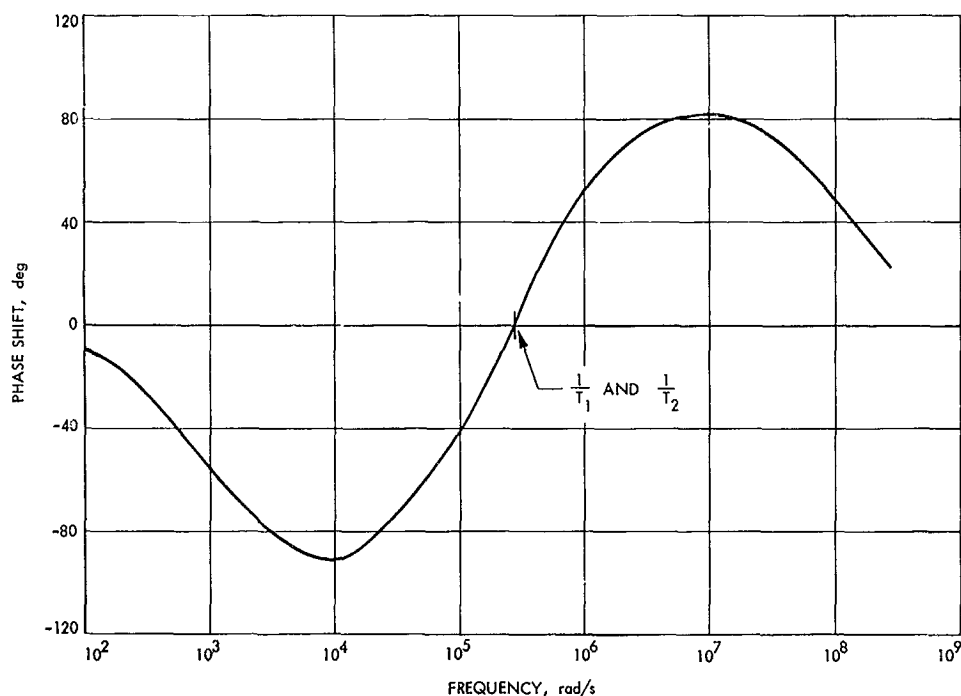


Fig. 3. Phase shift of lead-lag network

The input current I_1 is assumed to be an impulse of magnitude Q . By changing to the s domain and assuming $Z_2 \ll Z_1$, Eq. (1) becomes

$$E_2(s) = \frac{Q R_1}{C_f R_2} \left[\frac{sT}{(1 + sT)^2} \right] \quad (2)$$

where $T = T_1 = T_2 = 5 \mu s$. The inverse transform of Eq. (2) is

$$e_2(t) = \frac{Q R_1}{C_f R_2} \left[\frac{t \exp(-t/T)}{T} \right]$$

The peak voltage of the output pulse is

$$e_2(\text{peak}) = \frac{Q R_1}{e C_f R_2}$$

where $e = 2.718 = \text{natural logarithm base}$.

A peak output voltage greater than 1 mV was desired for the minimum detectable charge pulse ($2 \times 10^{-16} \text{ C}$). By choosing $C_f = 5.1 \text{ pF}$, which is a practical lower limit for this capacitor, the minimum peak output voltage e_2

becomes 2.88 mV. For a pulse of $2 \times 10^{-14} \text{ C}$, the maximum peak output voltage is 0.288 V. With a $\times 4$ buffer amplifier, the pulse amplitude range is approximately 0.0115 to 1.15 V.

6. Feedback Resistor R_f

Current in the attenuator is several orders of magnitude larger than that in Z_f . For this reason the time constant of Z_f does not significantly affect the preamplifier output pulse shape. Therefore, R_f can be chosen from noise considerations.

Feedback resistor R_f injects noise current into the first stage field-effect transistor (FET) with magnitude

$$i_n = \left(\frac{4 k T}{R_f} \right)^{1/2} \text{ A}/(\text{Hz})^{1/2} \quad (3)$$

where

$k = \text{Boltzmann constant} = 1.38 \times 10^{-23} \text{ J}/^\circ\text{K}$

$T = \text{temperature, } ^\circ\text{K}$

The channel noise of good quality n channel FETs is approximately $4 \times 10^{-14} \text{ A}$ at the frequencies of interest here (i.e., approximately 20–100 kHz). Equation (3) can

be rearranged to find the resistance that will produce this much current:

$$R_{f, \min} = \frac{4 k T}{i_n^2} \approx 10.4 \text{ M}\Omega$$

The actual value used in the breadboard preamplifier was 100 M Ω . Therefore, R_f is a negligible noise source.

7. FET Cascode Design

The input stage of the preamplifier uses a cascode configuration for several reasons.

- (1) Input capacitance, which is mostly unwanted Miller capacitance and likewise temperature sensitive, is decreased several orders of magnitude. Stability of these first two stages is thereby enhanced. This is important because the overall stability of the entire amplifier is critically dependent on the stability of each stage. The phase shift of each stage must be carefully controlled if the overall phase margin is to be adequate.
- (2) Bandwidth is also increased without sacrificing the superior low-noise characteristics of the first FET.

The cascode stage gain is simply the product of the common base stage (second FET) transconductance and the load resistance: $A_r = (3 \times 10^{-3}) (3 \times 10^3) = 9$.

To verify the gain and stability of the cascode configuration, an equivalent circuit of the stage was modeled for use with the ECAP computer-aided circuit-analysis program. This model is shown in Fig. 4. The results of this simulation, as run on the IBM 7094 computer, are shown in Figs. 5 and 6. The large gain and phase margins indicate a very good stability for the stage.

Since the two FETs in the cascode stage only provide a voltage gain of 9, the second stage must also be a low-noise device. A *p*-channel 2N2497 FET was chosen because it will also shift the dc bias level to zero. The following μ A709 needs this zero bias so that its output quiescent bias will be zero. Both the input node and the output node of the charge-sensitive amplifier are biased at zero. This allows dc-coupled feedback through the attenuator and R_f to achieve a high degree of dc stability. A 100% change in any single-loop gain parameter that affects bias will cause only a $100\% / 1.1 \times 10^5 = 0.00091\%$ change in the bias levels. The same stability is also achieved for the charge-to-voltage conversion gain of the amplifier. This gain is nominally $0.288 \text{ V} / 2 \times 10^{-14} \text{ C}$. The schematic of the complete charge-sensitive amplifier is shown in Fig. 7.

8. Initial Experimental Results

A breadboard version of the charge-sensitive amplifier has been fabricated and partially tested. The results of several of these tests are summarized.

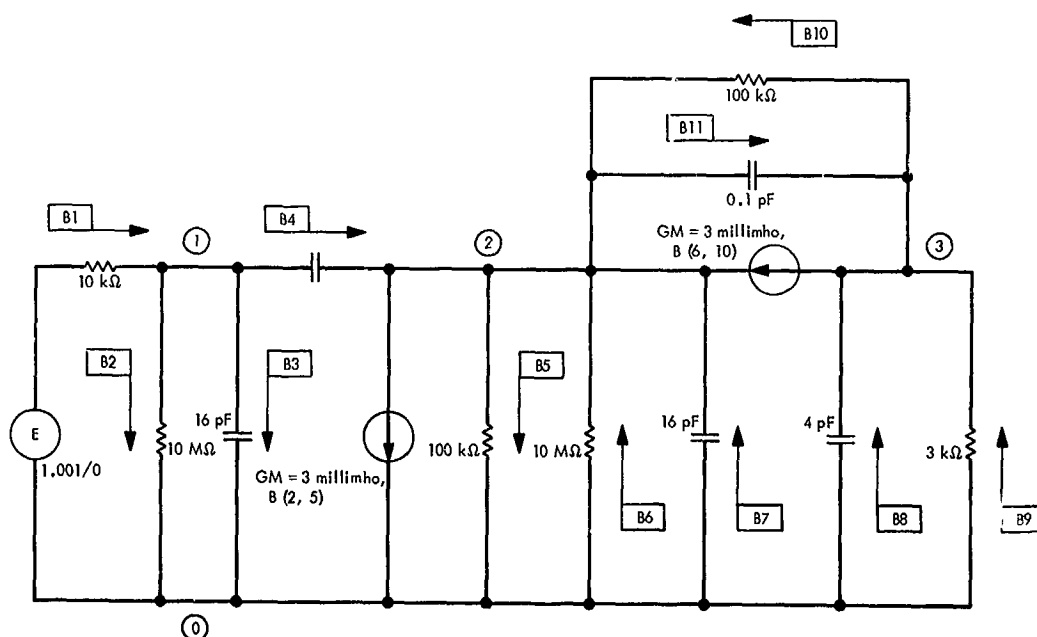


Fig. 4. 2N4869A FET cascode pair modeled for ECAP

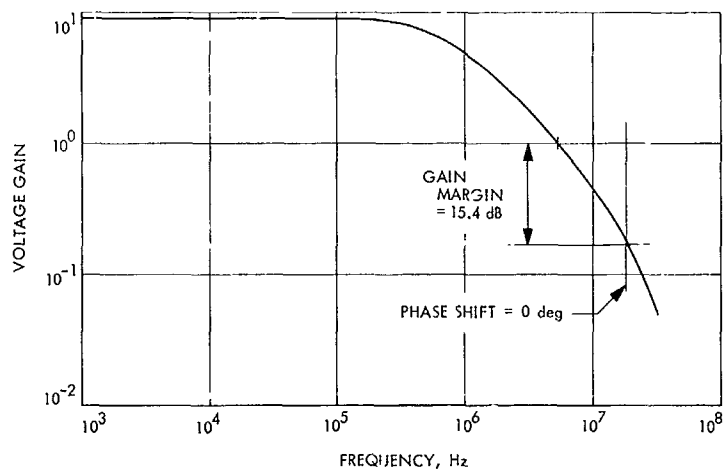


Fig. 5. Frequency characteristics of FET cascode stage

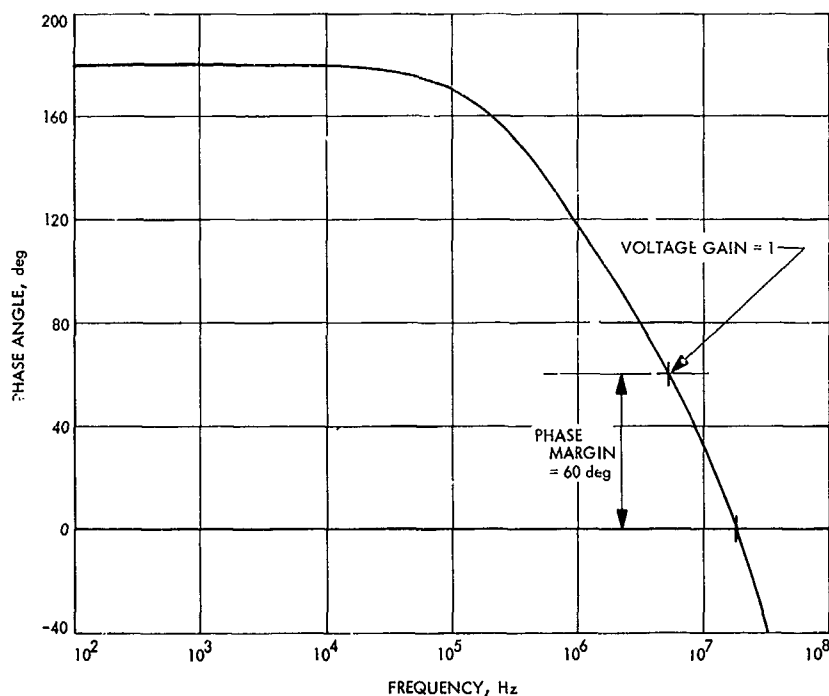


Fig. 6. Phase characteristics of FET cascode pair

Linearity test. By coupling to the input of the charge-sensitive amplifier through a 30-pF capacitor, the conversion gain can be measured. The charge transferred across the capacitor C is simply $Q = CV$, where V is the peak pulse voltage appearing on the generator side. The graph of peak voltage output (after the $\times 4$ buffer) as a function of charge input is shown in Fig. 8.

Noise test. Signal-to-noise ratio was measured at the preamplifier output terminal as a function of input stray

capacitance. The minimum stray capacitance of the device (in its present layout) is 35 pF. Coupled with this, a 30-pF output capacitance of an SEC camera tube would give a signal-to-noise ratio of 180.

Signal was defined as the peak pulse voltage resulting from the charge pulse input. Noise was measured by removing the generator and connecting a true rms voltmeter to the preamplifier output terminal. Figure 9 shows the results of this test.

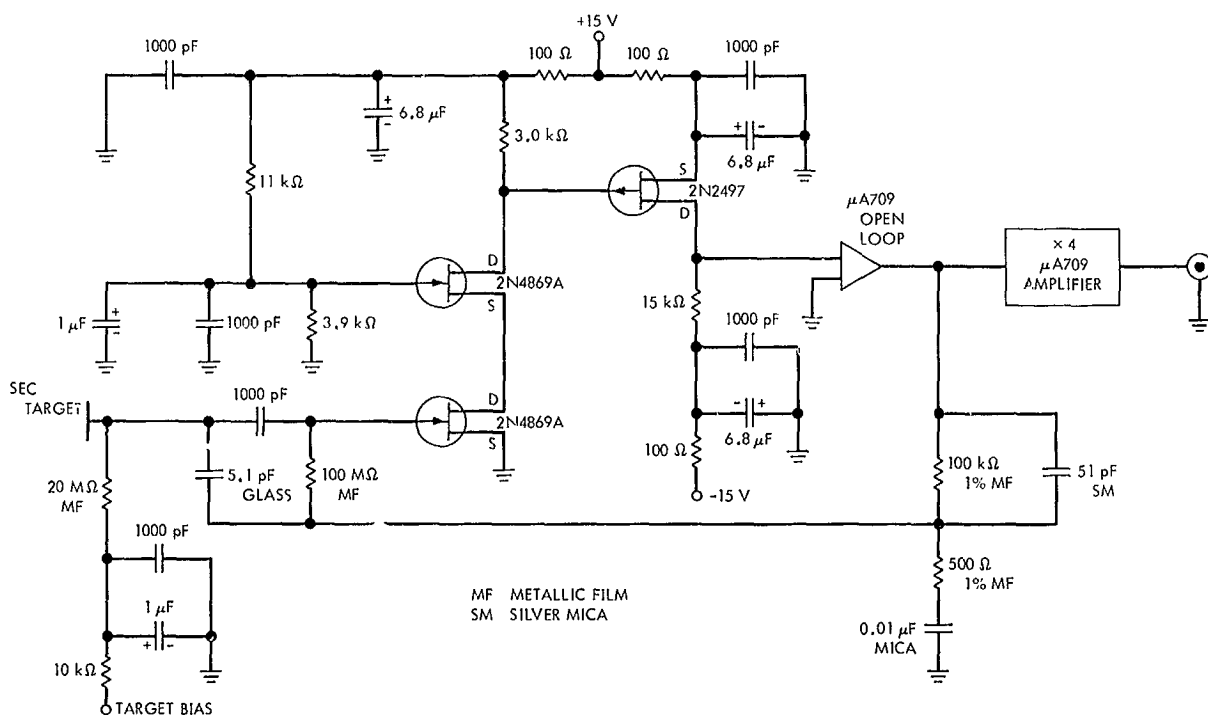


Fig. 7. Charge-sensitive amplifier

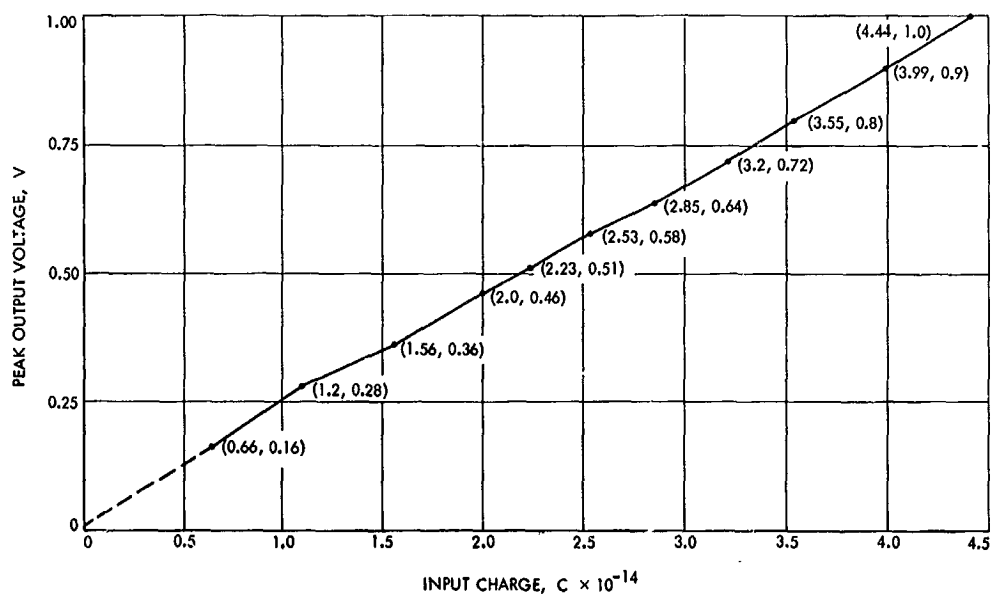


Fig. 8. Linearity of charge-sensitive amplifier

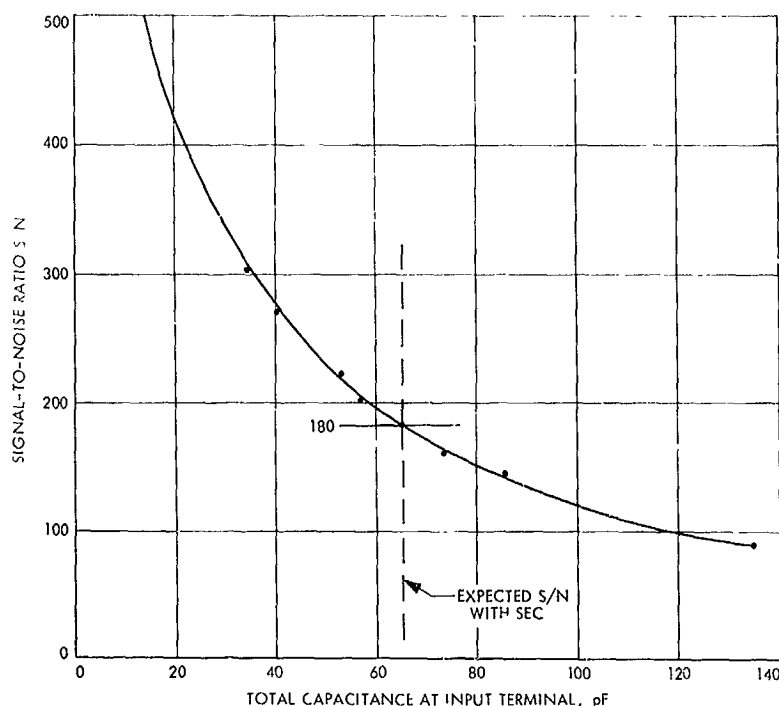


Fig. 9. Signal-to-noise ratio of preamplifier

9. Conclusions

The charge-sensitive preamplifier is capable of making the SEC camera tube compatible with a slow-scan television system. The circuit parameters chosen in this first iteration of such a device should be compatible with present *Mariner* television system timing parameters, i.e., 50-ms line time and 945 pixels/line. The dynamic range of the preamplifier covers the two orders of signal current magnitude expected for the above scan speed. Thus, charge pulses from 2×10^{-16} to 2×10^{-14} C/pulse will produce amplifier output pulses from approximately 0.010 to 1.0 V. The experimental preamplifier signal-to-noise ratio of 180 is adequate when coupled to the SEC camera tube that has a signal-to-noise ratio of only 50–100.

B. Alignment of the Flight-Model Infrared Interferometer, F. L. Murphy

1. Introduction

The design, development, and construction of the flight-model infrared interferometer were presented in SPS 37-43, Vol. IV, pp. 253–257, and SPS 37-52, Vol. III, pp. 142–148. In this article, the procedure in the optical alignment of the instrument is discussed in three areas:

(1) cat's-eye retroreflector, (2) fore-optics, and (3) servo-drive.

2. Cat's-Eye Retroreflector Alignment

Fabrication and assembly of the cat's eye constitute as much of the critical requirements as does the final optical test for focusing. Therefore, the mechanical assembly will be described along with optical alignment procedures.

The cat's-eye retroreflector consists of a secondary mirror assembly, quartz support tube, primary mirror, and differential thread adjustment housing. Its function, shown by the optical diagram in Fig. 10, is similar to that of a cube-corner reflector, namely to reflect rays in the direction opposite to their incidence.

The secondary mirror is placed at the approximate focal point of the primary mirror; its position must be maintained to within $1 \mu\text{m}$. Adjustment of the final position is accomplished by the differential thread adjustment of the primary mirror.

Since the rotation of the differential adjusting ring provides linear motion of the primary mirror, it was necessary to machine this assembly to the closest tolerance

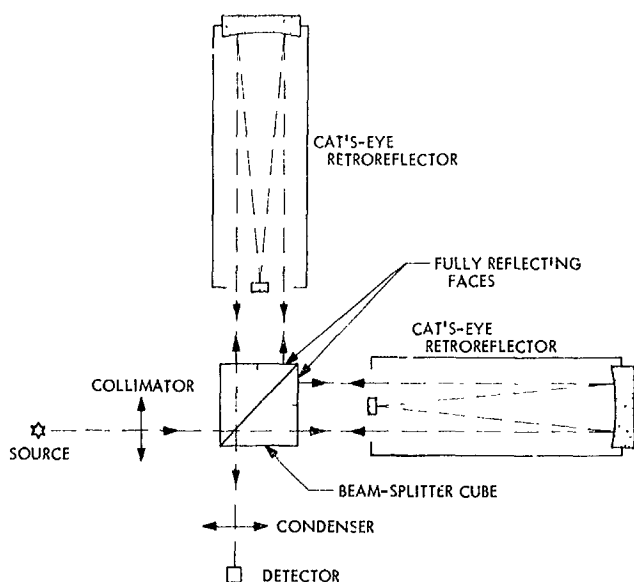


Fig. 10. Optical diagram of interferometer

possible, maintaining perpendicularity with the optical centerline and obtaining minimum backlash in the threads. To guarantee minimal backlash, the unit is spring-loaded. The quartz tube support was bonded into position with relation to the optical centerline while still on the machining spindle.

Assembly of the secondary mirror required the use of a fixture to accurately align the mirror, the piezoelectric transducer, the transducer support, and the quartz support while bonding as a unit.

The primary mirror is located 5.217 in. from the secondary mirror and must be positioned within 0.001 in. so that a minimum of differential thread movement would be required for the final adjustment. This positioning was verified by mechanical measurement.

The cat's eye was mounted on a special indexing head, providing bi-axial rotation and two-directional traverse, at the end of an optical bench. It was offset with respect to the bench centerline by one-half the radius of the quartz support tube. Alignment with the bench centerline required replacement of the primary mirror with an optical flat mirror of the same optical quality and then re-imaging a source upon itself.

A special fixture was used to hold the secondary assembly in position while making adjustments for proper placement. The secondary image was centered by observing it with a telescope from behind the primary mirror

through a small hole in its center. The secondary to primary mirror axes were held coincident within $0^{\circ}3'26''$ and, upon proper placement of the secondary, the fixture became a means for support during bonding. After bond curing, the fixture was removed and again the secondary image was viewed for verification of placement.

It had been thought that a vibrating Ronchi ruling test could be used for final primary to secondary mirror placement (SPS 37-43, Vol. IV), but this method proved to be of insufficient accuracy. The test did provide a means of calculating reflective loss through the cat's-eye system. Fine adjustment was done with the single cat's-eye interferometer arrangement as described in SPS 37-52, Vol. III.

3. Fore-optics Alignment

The fore-optics consist of seven 90-deg off-axis paraboloidal mirror segments, a chopper with half reflective and half transmitting window, two detectors, the photomultiplier, and the reference sources and black body source.

The function of the fore-optics is shown in Fig. 11, where the interferometer detector and reference detector alternately "see" the planet or the black body source as determined by the chopper window position.

The specifications require the incoming, as well as the black body, radiation to form an image on this chopper window of 1.1-mm diameter. This requires a 1.25-deg look angle. Therefore, the main alignment requirement was to have the four main mirror segments focus collimated radiation entering the aperture on the chopper window, and transmit this radiation to the interferometer normal to the beam-splitter face with an accuracy of ± 1 arc min.

The first approach to the alignment of the fore-optics was to align the planet-to-interferometer channel in relation to the chopper by means of an autocollimator. It had been hoped to reflect the collimator source in and out of the system by placement of an optical flat mirror in the interferometer at the beam-splitter position. This was not possible due to the large reflective losses through the autocollimator-fore-optics combination. Therefore, a laser module was placed and aligned on the interferometer centerline at the beam-splitter location and beamed through the planet-to-interferometer channel to the outside (Fig. 12), where a target and optical flat mirror were alternately viewed. When the planet-to-interferometer mirrors were aligned properly, the target showed on

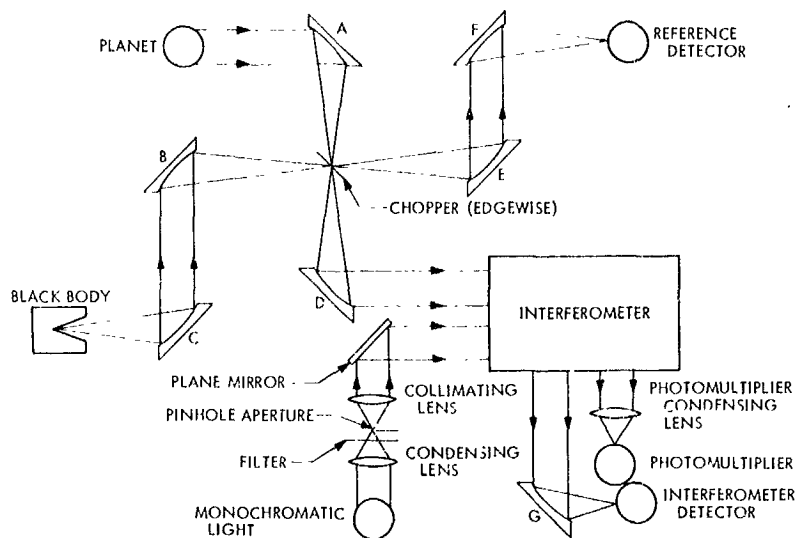


Fig. 11. Fore-optics of interferometer

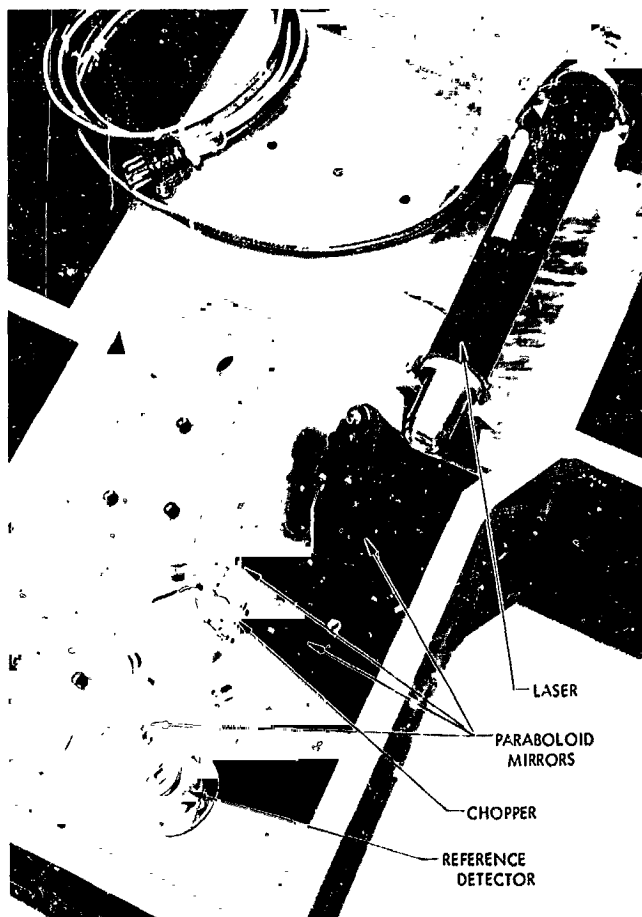


Fig. 12. Laser position for alignment

center and the mirror visually showed on center by reflecting the beam upon itself. The focal point in relation to the chopper window was obtained by both visual and mechanical measurement, using a laser beam expander.

With the laser module still in the beam-splitter position, the black body channel was also aligned by using the reflected half beam off the chopper window.

In order to align the reference detector channel, it was necessary to have an external source and observe the reflected beam from the chopper window. An external source is also necessary for placement of the servo-drive; therefore, another laser module was placed and aligned on the system optical centerline using the internal laser as its target. With both units on, the beams coincided.

The planet-to-interferometer channel alignment was verified with a photomultiplier, with the chopper running and forming a square-wave scope reading as shown in Fig. 13. Proper chopping was indicated by equal volume under the square wave, and proper focus was indicated by parallel sides forming the square wave.

With all channels satisfactorily aligned, the system was now ready for acceptance of the servo-drive. The internal laser was removed and the servo was completely assembled, except for the beam splitter, and placed into the system. The optically machined pads on this servo unit, which locate the beam-splitter cube in relation to the cat's eyes, were used for placement of an optical flat



Fig. 13. Square-wave chopper alignment verification

mirror to reflect the external laser beam upon itself when the servo-drive was in its proper place. To observe this, a pin hole was placed in the incoming target.

The beam-splitter cube was placed in position as was the phototube housing and reference sources. The infrared detector will not be placed into the system until after system testing. The external laser will be left in position and used as a source for system tests.

4. Servo-Drive Alignment

The servo-drive unit contains the cat's eyes, one of which is mounted into a moving housing that, when stepped, creates an optical path difference in relation to the stationary cat's eye. The unit locates the beam-splitter cube in relation to both cat's eyes.

The unit must function within the following specifications:

- (1) Provide 4 cm of optical path difference.
- (2) Maximum tilt of the optical axis of any optical element not to exceed 1 arc min from the normal to the beam splitter.
- (3) The lateral separation of the geometric axis of the elements not to exceed 0.5 mm.
- (4) Roll about the normal to the beam splitter of any optical element not to exceed 5 arc min.

The servo-drive was built and aligned by Aeroflex Laboratories. Alignment was observed and verified to fall

within the specifications except for the 4 cm of optical path difference, which was short by a negligible amount.

Alignment procedures were conducted with the use of an autocollimator and optical flat mirrors. With the main housing placed and leveled on an indexing head, the autocollimator was zeroed when viewing a mirror placed against the beam-splitter cube support pads perpendicular to the moving cat's-eye optical axis.

Neither the cat's eye nor the beam splitter was used during the alignment; instead, a fixture that simulated the weight and center of gravity of the cat's eye was mounted in the moving structure. Attached to the mounting surface of this structure was a mirror that defined the optical axis direction in relation to the beam-splitter pads, which indicated 15 arc sec from the normal. This was a total reading of the structure through its total travel.

The main structure was moved 90 deg and, viewing a mirror placed on the beam-splitter pads perpendicular to the stationary cat's-eye axis, a deviation of 9 arc sec was observed with relation to zero position. Placement of a mirror on the stationary cat's-eye mounting surface indicated 10 arc sec of deviation.

The autocollimator was shifted by means of a transfer mirror in order to observe a mirror placed on the moving structure and normal to its axis. Translating the moving structure to its extreme limits, roll was observed and found to be 5-arc sec deviation.

Lateral separation was measured by mechanical means and 0.002-in. deviation was found between all optical elements.

5. Present Status

The interferometer is now aligned as well as available techniques permit. System testing is in progress with reference fringes being produced by the instrument. As testing continues, it may be found that finer adjustment will have to be incorporated in order to obtain the desired final results.

XVII. Lunar and Planetary Sciences

SPACE SCIENCES DIVISION

A. Meteoritic Sampling of the Solar Wind,

H. C. Lord, III

The retention of low-energy ions incident upon silicate surfaces has been described in SPS 37-48, Vol. III, pp. 155-157. Furthermore, it was predicted that natural silicate samples exposed to a solar wind irradiation should retain both hydrogen and helium, the predominant solar wind species, Table 1 (Ref. 1).

A small number of meteorites have been known for some time to contain an inert gas fraction with an

isotopic and elemental composition essentially the same as the solar values. Furthermore, the helium concentration was on the order of 10^{-2} cm³/g, a factor of 10^3 greater than typical meteoritic helium concentrations. The meteorites containing this high concentration of unfractionated gas do not belong to any particular type, but rather only show in a typical light-dark structure. It is found that this solar primordial fraction is present only in the dark phase. Chemically the phases are essentially the same except for trace element variations and an enrichment of carbon in the dark phase.

Table 1. Pertinent solar wind parameters

Ion ^a	Average abundance	Average energy, keV
H ⁺	96.5 %	0.9
⁴ He ²⁺	4.4 %	1.8
⁴ He ¹⁺	3.0×10^{-3} ⁴ He ²⁺	3.6
³ He ²⁺	1.3×10^{-3} ⁴ He ²⁺	1.3
O	1.5×10^{-2} to 4×10^{-2} ⁴ He ²⁺	2.4 (¹⁶ O ⁶⁺)
^a No other elements have been definitely identified, but both C and Ne appear to be present.		

Eberhardt, et al. (Ref. 2), when studying separated minerals and grain sizes in Khor Temiki, discovered that HF etching of the individual grains radically reduced the gas concentration. Furthermore, the primordial gas content (in cm³/g) was found to decrease with increasing grain size. These characteristics suggest that a low-energy particle irradiation, like the solar wind, was the cause.

An 87.2-mg sample of Pesyanoe (a known solar primordial gas containing meteorite) was heated in 100°C steps, with the evolved gas at each step measured with a thermal conductivity detector gas chromatograph. The gas release results are shown in Fig. 1; as seen, both

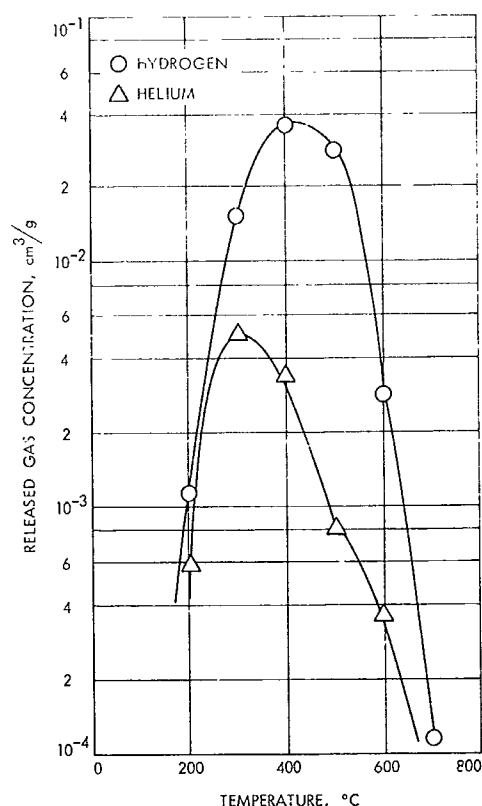


Fig. 1. Differential gas release from Pesyanoe

hydrogen and helium were detected. The absolute concentrations of each species observed is listed in Table 2, along with the results of a separate analysis. The He/H value obtained is compared with other pertinent extraterrestrial values. This He/H value of 0.061 is seen to be the same order of magnitude as that expected for the solar wind. The integrated gas release curves of the hydrogen and helium in Pesyanoe can be compared with the results obtained for low-energy ion injection into forsterite (SPS 37-48, Vol. III). It is seen that the curves are essentially the same.

Table 2. Gas composition of Pesyanoe solar wind

Source	Helium, cm ³ /g	Hydrogen, cm ³ /g	He/H
This work ^a	1.0×10^{-2}	8.4×10^{-2}	0.061
Zahringer (Ref. 3)	0.7×10^{-2}	—	—
Solar	—	—	0.160
Solar, photosphere (Ref. 4)	—	—	0.090
Solar wind (Ref. 1)	—	—	0.045

^aError $\pm 20\%$.

Further work is now in progress to analyze other gas-rich meteorites as well as to study the isotopic composition of the released hydrogen. The solar D/H value is thought to be $< 4 \times 10^{-5}$ (Ref. 5), while the terrestrial value is 1.56×10^{-4} . Analysis of the solar wind component will then give a value for the solar corona. It is proposed that detection of solar wind implanted hydrogen and helium is an unambiguous identification for extraterrestrial material. This is the first reported detection of solar wind hydrogen in extraterrestrial material.

References

1. Bame, S. J., et al., "Solar Wind Ion Composition," *Phys. Rev. Lett.*, Vol. 20, pp. 393-395, 1968.
2. Eberhardt, P., Geiss, J., and Grogler, N., "Further Evidence on the Origin of Trapped Gases in the Meteorite Khor Temiki," *J. Geophys. Res.*, Vol. 70, pp. 4375-4378, 1965.
3. Zahringer, J., "Ueber die Uredelgase in den Achondriten Kapoeta und Staroe Pesjanoe," *Geochim. Cosmochim. Acta*, Vol. 26, pp. 665-680, 1962.
4. Neugebauer, M., and Snyder, C. W., "Mariner II Observations of the Solar Wind: I. Average Properties," *J. Geophys. Res.*, Vol. 71, pp. 4469-4484, 1966.
5. Kinman, T. D., "An Attempt to Detect Deuterium in the Solar Atmosphere," *Mon. Not. Roy. Astron. Soc.*, Vol. 116, p. 77, 1956.

XVIII. Bioscience

SPACE SCIENCES DIVISION

A. Organic Analysis of Soil by Pyrolysis—Gas Chromatography—Mass Spectrometry—A Candidate Experiment for a Mars Lander, *P. G. Simmonds, G. P. Shulman, and C. H. Stenbridge*

1. Introduction

One of the experiments suggested for the unmanned biological exploration of Mars involves the organic analysis of the Mars soil by an automated pyrolysis-gas chromatography-mass spectrometry system¹ (Refs. 1, 2, and 3). The proposed experiment consists of the following basic steps:

- (1) A sample is heated in an inert atmosphere at a temperature sufficient to degrade and/or volatilize the organic matter present.
- (2) The complex mixture of volatile products is then fractionated by gas chromatography and the individual components identified by mass spectrometry.
- (3) The chemical composition of the organic matter contained in the original sample is inferred from the type of volatile pyrolysis compounds obtained and the pyrolysis conditions.

¹The Biological Exploration of Mars—A Plan for the First Three Missions. Edited by H. Ford, Aug. 1967 (JPL internal document).

This system not only offers the advantage of operational simplicity as compared to wet chemical procedures of the kind normally used for the analysis of soils and sediments (Ref. 4), but also permits investigation of normally intractable polymeric materials such as humic acid. A California desert soil containing less than 1% organic matter was selected as a suitably complex test sample to study the feasibility of the technique for the bio-organic analysis of soils.

2. Experimental Technique

A schematic of the laboratory apparatus is shown in Fig. 1. It should be understood that the present experimental arrangement is designed for analytical convenience and is intended to provide only the fundamental guidelines for a flight instrument. Experimentally, a 15 mg sample of desert soil containing 0.34% organic matter (Allison method, Ref. 5) was placed in a 3×0.159 cm OD stainless steel tube that was sleeved by a small pyrolysis furnace. This sample tube was connected directly to a 152×0.0005 m ID capillary column via a stainless-steel swagelock union. Carrier gas entered the sample tube through a capillary gas line that is silver soldered into the small volume union at its mid-point. The chromatographic column was coated with a 10% solution of DC200 silicone/Igepal C0990 (20:1) (Ref. 6). The sample tube was heated to 500°C in 15 s by the pyrolysis furnace

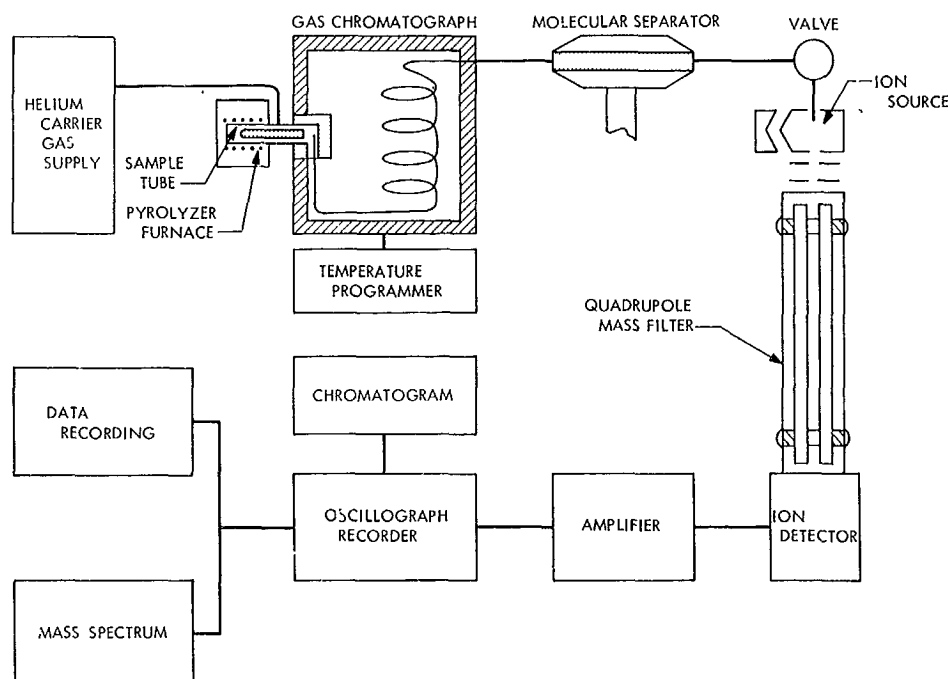


Fig. 1. Pyrolysis-gas chromatograph-mass spectrometer system

and the pyrolysate passed into the column under flow of helium. The column was temperature programmed from 30–185°C at 4°/min, and the eluted sample passed through a single-stage molecular separator (Ref. 7) directly into the ion source of an Electronic Associates, Inc. quadrupole mass spectrometer. The mass spectrometer was adjusted to scan the mass range 10–250 atomic mass units. An ion-current detector monitored the mass range of interest, and the output signal was displayed on a potentiometric recorder that served as a measure of the chromatographic peak intensity. The mass spectra were recorded simultaneously on an oscillograph and six-channel tape system. The tape storage system can subsequently be subjected to automated data processing for spectral recognition by a computer technique developed for mass spectrometry systems (Refs. 8, 9, and 10). The individual pyrolysis products separated by the gas chromatograph were identified by a comparison of their mass spectrometric fragmentation patterns with those in a reference library.

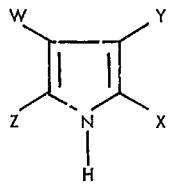
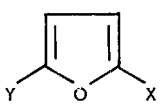
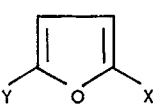
3. Results and Discussion

In order to reconstitute the identity of the principle classes of organic compounds present in the original sample, pyrolyses of pure compounds of biological interest were performed. A library of representative pyrolysis fragments can now be established for the thermal degradation of the major classes of terrestrial bio-organic

matter. Table 1, which summarizes this data, was compiled from both work performed in this laboratory and comprehensive literature surveys.

When pyrolysed, amino acids generally lose carbon dioxide to yield an intermediate amine that dehydrogenates to form the corresponding nitrile in high yield. Alternative decomposition by deamination and reduction yields the alkyl or aryl residues of the original amino acids (Refs. 11–14) or their decarboxylation products. Peptides and proteins yield the same major components identified from free amino acids. Carbohydrates decompose smoothly to a series of furans including furfural and furfuryl alcohol (Refs. 15 and 16). As a general rule, lipids (Ref. 17) form a series of alkenes and alkanes; e.g., tristearin pyrolyses to acrolein in addition to a mixture of straight-chain C_2 – C_{18} alkenes and alkanes with the alkenes predominating, except C_{17} , as expected. The presence of iron-containing minerals causes some cyclization and isomerisation during pyrolysis of lipids. Porphyrins thermally fragment to a series of pyrroles characteristic of the class (Refs. 18 and 19). Hydrocarbons decompose to lower molecular weight aromatic and aliphatic hydrocarbons, with a high degree of unsaturation (Refs. 20 and 21). When pyrolysed, the purine and pyrimidine bases of nucleic acids decompose extensively to form acetonitrile, methacrylonitrile and substantial amounts of hydrogen cyanide (Ref. 22); the carbohydrate moiety of

Table 1. Analysis of bio-organic compounds

Class of compound	Typical degradation products	Class of compound	Typical degradation products
Polypeptide and free amino acids ^a	RCH_2 , $RCH=CH_2$, RCN , $RCH=CH-CN$ $\begin{array}{c} R-CH_2 \\ \\ -HN-C-CO- \\ \\ H \end{array}$ <p>Note: R = aromatic, heteroaromatic, aliphatic, or substituted aliphatic</p>	Porphyrin ^d	 <p>And lower aliphatic nitriles, aliphatic-branched alkenes and alkanes</p> <p>Note: X, Y, W or Z = H or alkyl</p>
Carbohydrate ^b	 <p>And aliphatic ketones and aldehydes</p> <p>Note: X or Y = H, CH_3, CHO, or CH_2OH.</p>	Hydrocarbon ^c	$R(CH_2)_n-1-CH=CH_2$, $R(CH_2)_{n-1}-CH_3$, etc. <p>Note: R = aromatic, aliphatic, straight chain, or branched</p>
Lipid ^c	$CH_2=CH-CHO$, and straight-chain alkenes and alkanes $R(CO_2)_2C_3H_5$	Nucleic acid ^e	 <p>HCN, $=CH_2=C-CN$, and CH_2CN, NH_2, CH_3</p> <p>Note: X or Y = H, CH_3, CHO, and CH_2OH</p>
^a References 11, 12, 13, 14. ^c Reference 17. ^e References 20, 21. ^b References 15, 16. ^d References 18, 19. ^f Reference 22.			

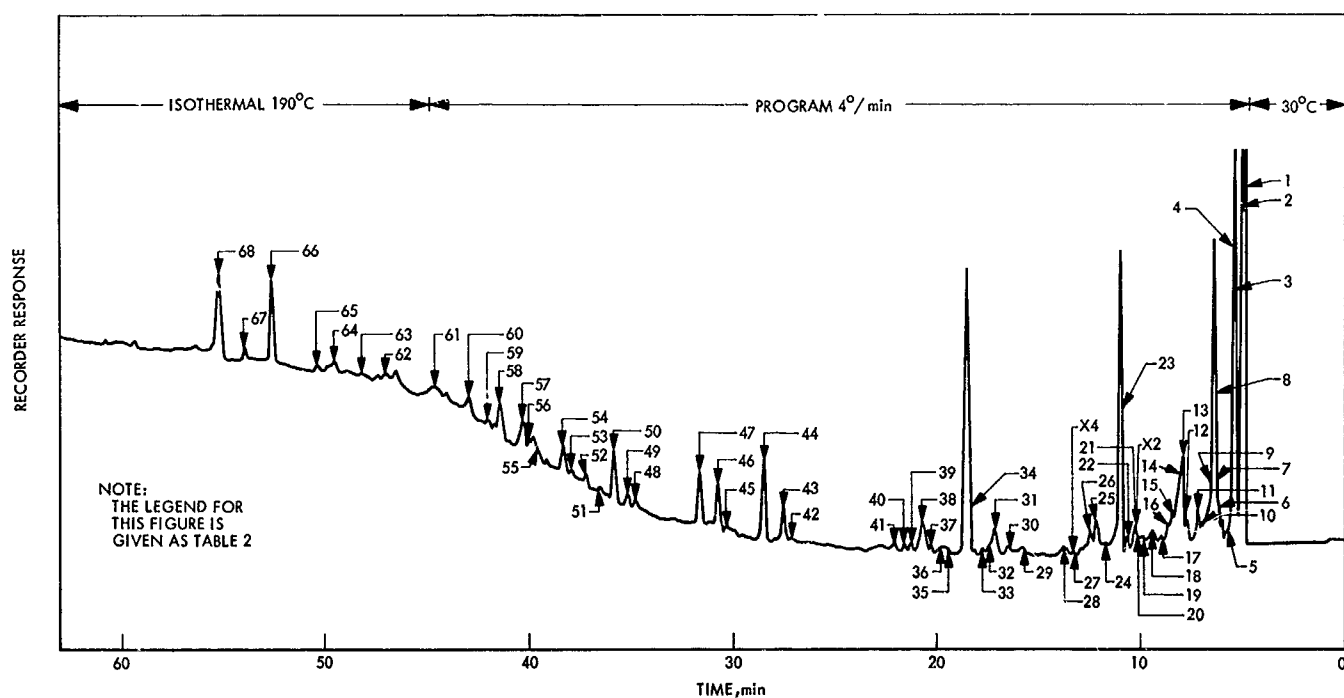


Fig. 2. Gas chromatograph of desert soil pyrolysate

nucleotides decompose as expected to substituted furans. At present, it is not possible to characterize the individual nucleic acid base.

A chromatogram of the pyrolysis products of the desert soil sample is shown in Fig. 2. These compounds are listed in Table 2, which is keyed to the peaks shown in Fig. 2. Identification of individual compounds was made by comparison of their mass spectra with the spectral library. Peak number 34 (Fig. 2), identified in Table 2 as toluene, represents approximately 2.5×10^{-8} g of material. In Table 3 the various pyrolysis fragments have been assigned to those classes of compounds from which they probably originated. In most cases, there is at least one characteristic series of products for each class. For example, aliphatic nitriles are formed by thermal degradation of amino acids, whether free or part of a polypeptide chain. It is apparent, however, that certain products such as the aliphatic alkanes and alkenes may originate from more than a single class of compound. For example, the identification of butene is *prima facie* evidence of the presence of polypeptide, lipid, or hydrocarbon classes; however, if a series of aliphatic and ring-substituted

aliphatic nitriles are detected in addition to butene, then it becomes more reasonable to infer the presence of either polypeptides or free amino acids. An alkene with a carbon number greater than C_6 dictates a choice between lipids and hydrocarbons. These may be distinguished readily since naturally-occurring hydrocarbons contain large amounts of aromatic or branched aliphatic structures, in contrast to the fatty acid pyrolysate.

Certain pyrolysis products appear to be specific for a single class of compound. Thus, phenylacetone nitrile is an exclusive product of phenylalanine and of polypeptides containing this amino acid. Similarly, indole and methyl indole have been observed only in tryptophan pyrolyses. Disubstituted pyrroles are characteristic for porphyrins, while the lower aliphatic mercaptans are, apparently, unique thermal fragments from the sulfur-containing amino acids. It is conceivable that mercaptans may also originate from hydrocarbon material with a high indigenous sulfur content; however, in this case, some aromatic sulfur compounds would also be expected. Furans and substituted furans are characteristic for carbohydrate moieties.

Table 2. Compounds identified from gas chromatograph of desert soil pyrolysate (Fig. 2)

Peak No.	Compound	Peak No.	Compound	Peak No.	Compound
1	Carbon dioxide, methane ethane	23	Benzene	46	Styrene
2	Propene, carbonyl sulfide	24	2-butenal	47	2-furaldehyde
3	Butene, hydrogen sulfide	25	Dimethyl furan	48	Unidentified
4	Methanethiol, methyl propane, dimethyl sulfide	26	Methyl pentene	49	Dimethyl hexadiene
5	Methyl butene	27	Unidentified	50	Isopropyl benzene + unidentified
6	Propanal, methanol	28	Hexene	51	Unidentified
7	Acrolein	29	Unidentified	52	Methyl styrene
8	Furan, acetone	30	Dithiabutane	53	Unidentified
9	2-methyl propanal	31	C_6 branched alkane	54	Methyl furaldehyde
10	Butanone	32	Pyrrole	55	Unidentified (amine)
11	Dimethyl butene	33	Unidentified	56	C_6 olefin
12	Methyl propenal	34	Toluene	57	Furfuryl alcohol
13	Ethanenitrile	35	Methyl pyrrole	58	Benzonitrile
14	Acrylonitrile	36	Unidentified	59	Indene
15	Pentene	37	C_7 branched alkene	60	Phenyl acetone nitrile
16	2-methyl furan	38	Unidentified	61	Phenol
17	Butanal	39	Dimethyl pentene	62	o- or m cresol
18	Pentanone propanenitrile	40	Dimethyl pyrrole	63	p-cresol
19	Methyl butadiene	41	Pyridine	64	Dimethyl phenol
20	Methacrylonitrile	42	Methyl pyridine	65	Unidentified
21	Valeraldehyde	43	Ethyl benzene	66	Alkyl benzene
22	Butanenitrile	44	Dimethyl benzene	67	Alkyl phenol
		45	2-methyl pyrazine	68	Indole

Table 3. Assignment of pyrolysis fragments to biological classes

Protein ^a	Carbohydrate ^a	Nucleic acid	Lipid		
			Fats and waxes ^a	Hydrocarbon	Porphyrin ^a
Characteristic series					
Ethane nitrile Acrylonitrile Propanenitrile Methacrylonitrile Butanenitrile Benzonitrile Phenylacetoneitrile Ethene Propene Methylpropane Methylbutene Methylpentene Benzene Toluene Ethylbenzene Styrene Propylbenzene Methylstyrene	Acrolein Propanal Acetone 2-methylpropanal Butanone 2-methylpropanal Butanal Pentanone Pentanal 2-butenal Furan 2-methylfuran Dimethylfuran Furfural Methylfurfural Furfuryl alcohol		Ethene Propene Butene Pentene Hexene C ₆ alkene C ₇ alkene C ₉ alkene		Pyrrole Methylpyrrole Dimethylpyrrole C ₆ alkene C ₇ alkene C ₈ alkadiene C ₉ alkene
Individual compounds					
Phenol ^b Cresols ^b Xylepol ^b Indole ^b Indene Methanethiol ^b Dimethyl sulfide ^b Dimethyl disulfide ^b Pyrrole Methylpyrrole Pyridine Methylpyridine	Methylbutadiene Benzene	Methanol ^b Acrylonitrile Ethanenitrile Methacrylonitrile Butanenitrile Pyridine Methylpyridine 2-methylpyrazine ^b	Acrolein ^b	Dimethylbenzene Alkylbenzene Methylpentene Dimethylbutene	
^a Presence established. ^b Characteristic.					

4. Conclusion

A considerable amount of work remains to be done in establishing the precise pyrolytic pathways and mechanisms of pyrolysis for specific macromolecules of biological interest. It is anticipated that detailed studies of this kind will establish a substantial library of thermal fragments unique to the pyrolysate of a single bio-organic class, and, more specifically, to individual members of the class. Based on the above observations and a critical study of the individual pyrolysis products from Table 3, it is possible to infer that all the biochemically important classes of compounds are present in the desert soil sample. This is not surprising since microbiological surveys in this area have clearly established the existence of approximately 5×10^7 microorganisms per gram of soil (SPS 37-34, Vol. IV, pp. 193-202). The present work is sufficiently encouraging to justify the conclusion that the primary objectives of the pyrolysis-gas chromatography-mass spectrometry experiment are attainable. A preliminary investigation of the Precambrian Fig Tree shale (age 3.1×10^9 yr) by this technique indicates that the pyrolysate is, predominately, a mixture of hydrocarbons with a surprising lack of any heteroatom fragments. This work will be continued to include other shales and also meteorites and will be reported in a future article.

References

1. Oyama, V. I., *Proceedings of the Thirteenth Lunar and Planetary Exploration Colloquium*, Vol. 3, Part 2, p. 29, North American Aviation S&ID, Downey, Calif., 1963.
2. Bentley, K. E., *et al.*, *AAS Sci. Tech.*, Vol. 2, p. 93, 1964.
3. Rea, D. G., National Academy of Sciences Publication 1296, p. 347, 1966.
4. Degens, E. T., and Reuter, J. H., in *Advances in Organic Geochemistry*, No. 15, p. 377. Edited by U. Colombo and G. D. Hobson. The MacMillan Company, New York, 1964.
5. Allison, L. E., *Soil Sci. Soc. Amer. Proc.*, Vol. 24, p. 36, 1960.
6. Teranishi, R., and Mon, T. R., *Anal. Chem.*, Vol. 36, p. 1490, 1964.
7. Ryhage, R., *Anal. Chem.*, Vol. 36, p. 759, 1964.
8. Boettger, H. G., "Automated Data Reduction of High-Resolution Mass Spectra of Organic Compounds," Abstract 233, presented at Pacific Conference on Chemistry and Spectroscopy, Anaheim, Calif., 1967.
9. Boettger, H. G., "An Advanced Data Processing System for Fast Scanning High-Resolution Mass Spectrometers," Paper 31, presented at the fifteenth Mass Spectrometry and Allied Topics Conference, Denver, Colo., 1967.
10. Hites, R. A., and Biemann, K., *Anal. Chem.*, Vol. 40, p. 1217, 1968.
11. Kanomata, K., and Mashiko, Y., *Nippon Kagaku Zasshi*, Vol. 87, p. 57, 1966.
12. Vollmin, J., *et al.*, *Microchem. J.*, Vol. II, p. 73, 1966.
13. Merritt, C., Jr., and Robertson, D. H., *J. Gas Chromatography*, Vol. 5, p. 96, 1967.
14. Shulman, G. P., and Simmonds, P. G., *Chem. Comm.*, p. 1040, 1968.
15. Kata, K., *Arg. Biol. Chem.*, Vol. 31, p. 657, 1967.
16. Kata, K., and Komorita, H., *Arg. Biol. Chem.*, Vol. 32, p. 21, 1968.
17. Janak, J., *Nature*, Vol. 185, p. 684, 1960.
18. Levy, R. L., *et al.*, *J. Gas Chromatography*, Vol. 2, p. 254, 1964.
19. Whitten, D. G., Bentley, K. E., and Kuwada, D., *J. Org. Chem.*, Vol. 31, p. 322, 1966.
20. Holman, R. T., Deubig, M., and Hayes, H., *Lipids*, Vol. 1, p. 247, 1966.
21. Henderson, W., *et al.*, *Nature*, Vol. 219, p. 1012, 1968.
22. Jennings, E. C., and Dimick, K. P., *Anal. Chem.*, Vol. 34, p. 1543, 1962.

XIX. Physics

SPACE SCIENCES DIVISION

A. Jupiter's Red Spot and the Solar Wind,

M. Eikrem¹ and M. Neugebauer

During the past few months, there have been some interesting discussions in the scientific literature concerning the possible origin of variations in the intensity of Jupiter's red spot. First, Graf, Smith, and McDevitt (Ref. 1) suggested that the red-spot variations were correlated with the Zurich sunspot number; the data on which their argument was based are shown in Fig. 1. The suggested coupling agent was the ultraviolet radiation associated with solar activity.

The fact that the red-spot data have at least two maxima per 11-yr solar cycle led T.S. Smith (Ref. 2) to suggest that solar flare protons are a more probable cause of variations in the red spot. However, Jupiter's strong magnetic field may prevent all but the highest rigidity protons from reaching the relatively low magnetic latitude of the red spot.

Further analysis at JPL has led to the suggestion that variations in the solar wind, rather than in solar flare protons or ultraviolet radiation, may be the cause of red-spot variations. Because no direct measurements of the

solar wind were made before the current decade, geomagnetic activity was selected as a measure of the solar wind. Although the details of the interaction of the solar wind with the earth's magnetic field are not yet completely clear, the mechanism which converts solar wind variations into geomagnetic activity, auroral activity, and enhanced precipitation of geomagnetically trapped radiation should also operate at Jupiter, if the solar wind exists at 5 AU. The location and shape of the Jovian red spot are suggestive of a magnetic anomaly at which enhanced precipitation of trapped particles might occur (similar to the earth's south Atlantic anomaly).

In Fig. 2, the red-spot intensity and geomagnetic data are plotted together versus time for the years 1892 through 1947. For each opposition of Jupiter with the earth and sun, the red-spot intensity is given by Peek's (Ref. 3) quantitative index, which ranges from 0 = invisible to 8 = "dark and conspicuous," and geomagnetic activity is represented by a 2-mo average of the geomagnetic character index C_4 (Ref. 4) for the month of and the month preceding the opposition. This particular 2-mo average was chosen because at opposition the earth and Jupiter sample nearly the same radially flowing solar wind plasma with a 10- to 20-day time delay required for the plasma to travel from the orbit of earth to the orbit of Jupiter.

¹JPL summer employee.

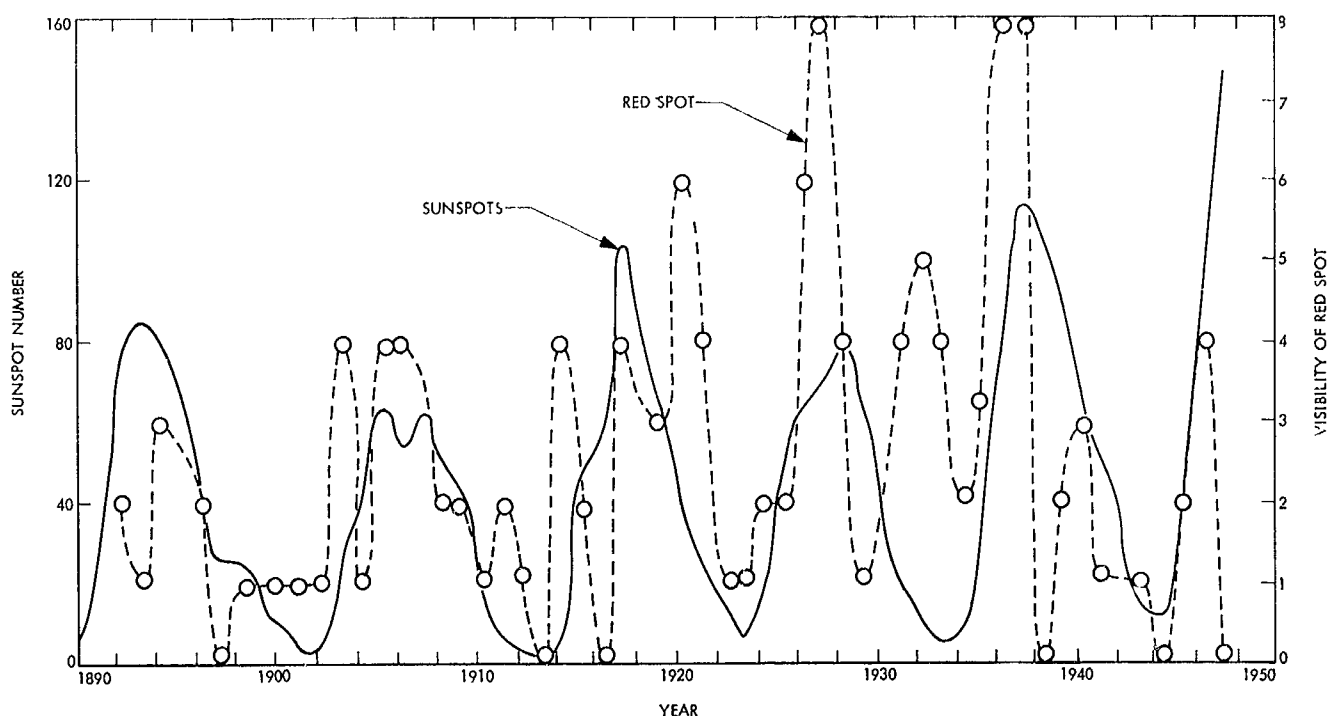


Fig. 1. Smoothed yearly-average Zurich sunspot number and relative intensity of Jovian red spot between 1892 and 1947

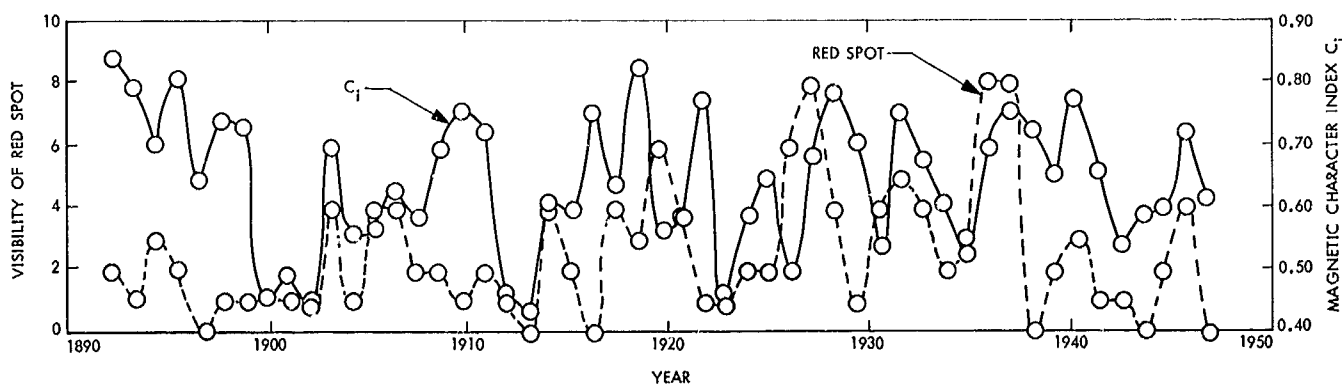


Fig. 2. Two-month average geomagnetic character figure C_i and relative intensity of Jovian red spot between 1892 and 1947

Figure 2 shows a fairly convincing correlation between the 2-mo C_i and red-spot intensity for the years 1900–1908, and after 1922. The yearly-average C_i (not plotted) correlates very well the red-spot data before 1900. For those intervals, the C_i –red spot correlation is appreciably better than the corresponding sunspot–red spot correlation shown in Fig. 1.

Recently, it has been suggested that the termination of the solar wind by a shock transition to subsonic flow

may occur as close to the sun as ~ 5 AU, or the orbit of Jupiter (Ref. 5). It is tempting to speculate that the years 1909–1911, 1916, 1918, and 1922, which show no correlation between C_i and red-spot intensity, correspond to periods when Jupiter was outside the shock. The fact that the periods of very poor correlation are generally periods of low red-spot intensity supports this speculation.

In conclusion, although the data in Fig. 2 do not show a statistically significant correlation between the red-spot

intensity and C_1 for the entire period 1891–1947, the correlation during some periods is quite striking. The resultant suggestion that the great red spot is associated with a magnetic anomaly could be tested by proposed spacecraft missions to Jupiter.

References

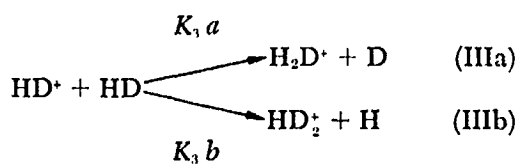
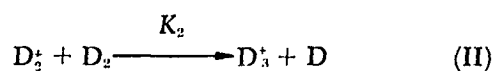
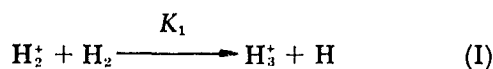
1. Graf, E. R., Smith, C. E., and McDevitt, F. R., *Nature*, Vol. 218, p. 857, 1968.
2. Smith, T. S., *Nature*, Vol. 219, p. 357, 1968.
3. Peek, B. M., *The Planet Jupiter*. Faber and Faber, Ltd., London, England, 1958.
4. *Handbook of Geophysics and Space Environments*. Air Force Cambridge Research Laboratories, Bedford, Mass., 1965.
5. Hundhausen, A. J., *Planet. Space Sci.*, Vol. 16, p. 783, 1968.

B. An ICR Study of the Ion-Molecule Thermal Reaction Rates of H_2^+ , D_2^+ , and HD^+

D. D. Elleman, J. King, Jr., and M. T. Bowers

1. Introduction

The measurement of the ion-molecule thermal rates in the gas phase Reactions I–III has been of considerable interest for some time.



Harrison has developed a pulsing technique for studying thermal energy ion-molecule reaction rates and has reported thermal values for K_1 and K_2 (Refs. 1 and 2). (In private communication, Harrison later reported that these values for K_1 and K_2 are probably too low by a factor of 2.) Stevenson and Schiesler (Ref. 3) and Reuben and Friedman (Ref. 4) have used high pressure (hp) mass spectrometry to obtain rate constants at higher energies for Reactions I, II, and III.

This article reports the results of a study of reactions I–III, using ion cyclotron resonance (ICR) spectroscopy (Refs. 5, 6, 7, and SPS 37-53, Vol. III, pp. 149–151). A

brief description of the ICR spectrometer and of the ICR technique was given in SPS 37-46, Vol. IV, pp. 205–208.

2. Experimental Techniques

Previous work using ICR single resonance techniques has shown that it is possible to determine the thermal energy rates of ion-molecule reactions (Ref. 8 and Footnotes 2 and 3). A description of this technique will be given here so as to aid in the evaluation of the rate constants that are reported.

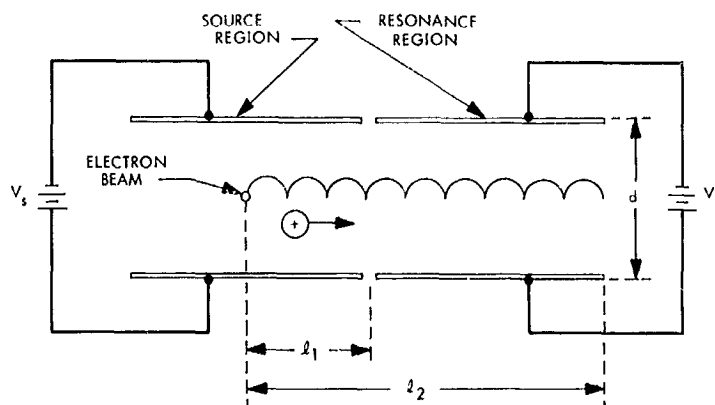


Fig. 3. Side view of ICR cell showing parameters for kinetic analysis (magnetic field is parallel to electron beam)

Figure 3 shows the geometry of the ICR cell required for a kinetic analysis. Separate drift voltages v_s and v_r are applied to the source and resonance regions of the cell. The arrow indicates the direction of ion drift for the crossed field geometry. The drift velocities (in m/sec) in the source and resonance regions are

$$v_{sd} = \frac{V_s}{Bd} \quad (1)$$

$$v_{rd} = \frac{V_r}{Bd} \quad (2)$$

where d is the spacing between the plates in meters, V_s and V_r are the voltages in practical volts across the plates, and B is the magnetic field in Wb/m^2 . If the effects of fringing fields are neglected, then the times at

¹Bowers, M. T., Elleman, D. D., and Beauchamp, J. L., *J. Phys. Chem.*, Vol. 72, p. 3599, 1968.

²Bowers, M. T., Elleman, D. D., and King, Jr., J., *J. Chem. Phys.* (in press).

which the ion enters τ and leaves τ' , the resonance region, are given by

$$\tau = \frac{l_1}{v_{rd}} \quad (3)$$

$$\tau' = \frac{l_1}{v_{rd}} + \frac{l_2 - l_1}{v_{rd}} \quad (4)$$

where l_1 and l_2 are shown in Fig. 3.

Beauchamp (Ref. 8) and Bowers, Elleman, and Beauchamp (Footnote 2) have developed an equation which relates the intensity of the primary ion I_p and secondary ion I_s to the reaction rate constant K in the limit where $nK\tau'_s \ll 1$ and $nK\tau'_p \ll 1$. The subscripts p and s on τ' refer to the primary and secondary ion exit times and n is the number of neutral molecules per unit volume in the cell. The resulting equation is

$$\frac{nK}{2} = \frac{1}{\left(1 + \frac{m_s}{m_p} \frac{I_p}{I_s}\right) (\tau'_p + \tau_p)} \quad (5)$$

where m_s and m_p are the masses of the secondary and primary ions, respectively. In the development of Eq. (5), it has been assumed that the line widths of the primary and secondary ions are equal; experiments to date have shown that this is a valid approximation.

It is convenient to rewrite Eq. (5) in terms of known instrument parameters when using the expression to measure the rate constant K . Generally, for ease of operation, the drift voltages in the source and resonance regions are set equal so that

$$V = V_R = V_s \quad (6)$$

It is then possible to express $\tau_p + \tau'_p$ in terms of known measurable quantities so that

$$\tau_p + \tau'_p = \frac{l_1 + l_2}{v_p} = \frac{B_p}{v} d(l_1 + l_2) \quad (7)$$

where B_p is the value of the magnetic field at the resonance condition for the primary ion. Equations (5) and (7) can be combined and simplified and the values for l_1 , l_2 , and d can be used to give

$$\frac{nK}{2} = \frac{V}{\left(1 + \frac{m_s}{m_p} \frac{I_p}{I_s}\right) B_p 2.224 \times 10^{-3}} \quad (8)$$

Data is then taken by varying the drift voltage V and measuring the resulting changes in the intensities I_p and I_s of the primary ion and secondary ion. A plot of

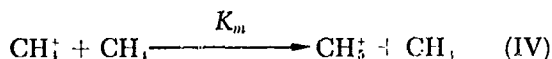
$$\left(1 + \frac{m_p}{m_s} \frac{I_p}{I_s}\right)^{-1}$$

versus V^{-1} is made and the slope S is obtained. Equation (8) is then rewritten in the form

$$\frac{nK}{2} = \frac{S}{2.24 \times 10^{-3} B_p} \quad (9)$$

The rate constant is then readily obtained from Eq. (9) if n , the number of neutral molecules per unit volume, is known.

The JPL spectrometer has been calibrated for n by measuring, with the technique described above, the well known rate constant of methane in the reaction



The value of n determined from the pressure measurement of the ionization gage attached to the cell was compared to the value of n calculated from the ICR-measured value of K_m and the accepted literature value of K_m .² It was determined that the ion gage value of n was low by a factor of 3.5, and all subsequent ion gage measurements of n have been corrected by this factor. Corrections for differences between the gage, calibrated for N_2 , and the sample gas are made by multiplying the ion gage reading by the ratio $\sigma_I(\text{N}_2)/\sigma_I(i)$, where $\sigma_I(\text{N}_2)$ is the ionization cross section of N_2 gas and $\sigma_I(i)$ the ionization cross section of the sample gas. It is assumed that the collection efficiency of the ion gage is equal for all ions.

The ICR experiments on hydrogen and deuterium were performed at a pressure of 2×10^{-6} torr; the gas was weakly ionized by a 45-eV electron beam of 0.1 μA . The resulting ion current down the cell was in the range of 1×10^{-11} A. The gases were Matheson Research grade and were used without further purification.

3. Experimental Results

The experimental plots for Reactions I-III are given in Fig. 4. As can be seen, a straight line that passes through the origin fits the experimental points for a relatively large range of V . The resulting rate constants calculated from

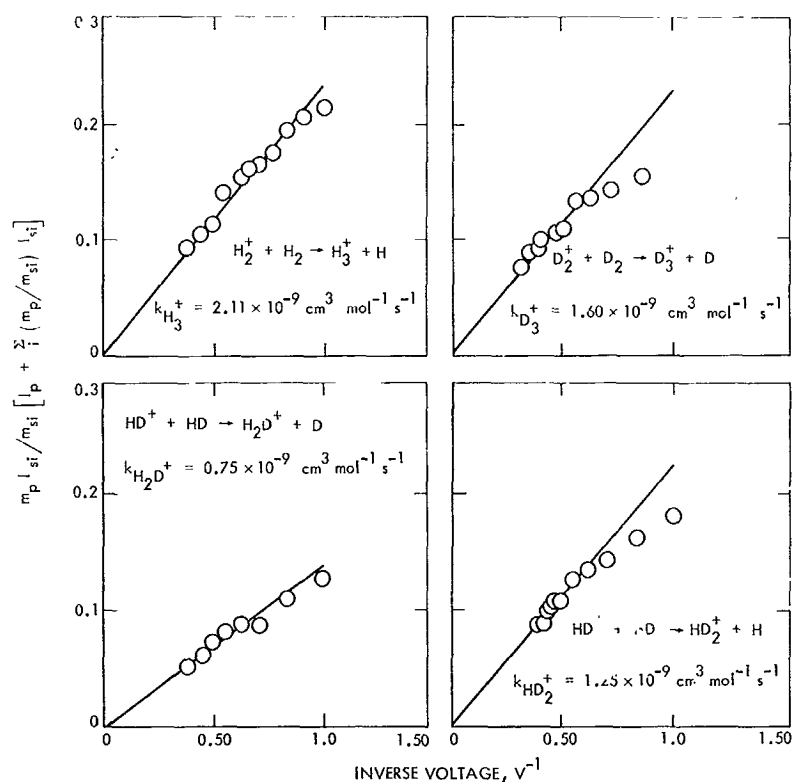


Fig. 4. $m_p I_{si} / m_{si} [I_p + \sum (m_p / m_{si}) I_{si}]$ vs (drift voltage) $^{-1}$ for various isotopic hydrogen reactions. (Straight line was used to determine rate constants according to Eq. 9)

this ICR data are listed in Table 1, along with data from other workers for comparison.

The values $K_1(\text{ICR})$ and $K_2(\text{ICR}) = 2.11$ and 1.6×10^{-9} $\text{cm}^3 \text{ molecule}^{-1} \text{ sec}^{-1}$ obtained from Fig. 4 are in good agreement with previously reported data. Harrison, et al.,

(Ref. 1) reported thermal rate constants obtained from pulsed work of $K_1(\text{pulse})$ and $K_2(\text{pulse}) = 0.59$ and $0.58 \times 10^{-9} \text{ cm}^3 \text{ molecule}^{-1} \text{ sec}^{-1}$. In a more recent paper, Gupta, et al. (Ref. 2) have reviewed many of the thermal rate constants reported in Ref. 1. Most of the proton transfer reactions in Ref. 1 were too low by a factor of approximately 2. While revised values of K_1 (pulse) and K_2 (pulse) were not reported by Gupta, et al. (Ref. 2), Harrison has indicated that the initially reported values in Ref. 1 are also probably too low by approximately a factor of 2. In addition, Harrison, et al. (Ref. 1) report $K_1(\text{pulse})/K_2(\text{pulse}) = 1.01$, compared with the value of 1.33 reported for that ratio here. Beuben and Friedman (Ref. 4) have reported $K_1(\text{hp})$ and $K_2(\text{hp}) = 2.02$ and $1.44 \times 10^{-9} \text{ cm}^3 \text{ molecule}^{-1} \text{ sec}^{-1}$ at 1.4-eV exit ion energy with $K_1/K_2 = 1.43$ in fair agreement with the ratio reported here. Reuben and Friedman (Ref. 4) also give values of K_1 and K_2 as a function of energy and report both K_1 and K_2 decrease with energy above 1.4-eV exit ion energy. The energy dependence of Reactions I-III as determined by ICR is quite complex, and the energy dependence results will be presented at a later date.

Table 1. Thermal reaction rate constants for H_2 , D_2 , and HD

Reaction	$K \times 10^{-9}, \text{cm}^3 \text{ molecule}^{-1} \text{ sec}^{-1}$			
	ICR	Pulse ^a	High pressure ^b	Theory ^c
$\text{H}_2^+ \rightarrow \text{H}_3^+$	2.11	0.59	2.02	2.08
$\text{D}_2^+ \rightarrow \text{D}_3^+$	1.60	0.58	1.44	1.45
$\text{HD}^+ \rightarrow \text{H}_2\text{D}^+$	0.75	--	0.75	1.66
$\text{HD}^+ \rightarrow \text{HD}_2^+$	1.25	--	0.91	

^aRef. 1. These values should probably be multiplied by approximately 2. See Ref. 2.
^bRef. 4. Data are the lowest energy reported (1.4-eV exit ion energy).
^cRef. 9.

The rate constants for the HD^+ reactions were determined to be K_a (ICR) and K_{ab} (ICR) = 0.75 and $1.25 \times 10^{-9} \text{ cm}^3 \text{ molecule}^{-1} \text{ sec}^{-1}$ with a ratio $k_a/k_b = 1.67$. Reuben and Friedman (Ref. 4) report values of K_a and $K_{ab} = 0.75$ and $0.91 \times 10^{-9} \text{ cm}^3 \text{ molecule}^{-1} \text{ sec}^{-1}$ with the ratio $K_a/K_{ab} = 1.21$. The agreement is fair.

The existence of a significant isotope effect in Reactions IIIa and IIIb indicates that either a relatively long-lived complex is formed in the hydrogen molecule-parent ion system or there is preferential orientation in a shorter-lived complex (Refs. 4, 10, and 11). There is evidence from photochemical studies (Ref. 12), however, that both a stripping mechanism and a complex mechanism are simultaneously occurring at low energies in Reactions I-III. The rate constants reported here merely reflect the total rate of formation of $(\text{H,D})_2^+$ ions from the $(\text{H,D})_2^+ + (\text{H,D})_2^+$ reactant at thermal energies.

References

1. Harrison, A. G., Myher, J. J., and Thynne, J. C. J., "Ion-Molecule Reactions in the Gas Phase," *Advan. Chem.*, Series 58, Chapt. 10, 1966.
2. Gupta, S. K., Jones, E. G., Harrison, A. G., and Myher, J. J., *Can. J. Chem.*, Vol. 45, p. 3107, 1967.
3. Stevenson, D. P., and Schiesler, D. O., *J. Chem. Phys.*, Vol. 29, p. 282, 1958.
4. Reuben, B. G., and Friedman, L., *J. Chem. Phys.*, Vol. 37, p. 1636, 1962.
5. Beauchamp, J. L., Anders, L. R., and Baldeschwieler, J. D., *J. Am. Chem. Soc.*, Vol. 89, p. 4569, 1967.
6. Baldeschwieler, J. D., *Science*, Vol. 159, p. 263, 1968.
7. Fluegge, R. A., *Cornell Aeronautical Lab Report UA-1854-P-1*, U.S. Department of Commerce Clearing House for Federal Scientific and Technical Information, Washington, D. C., Feb. 1967.
8. Beauchamp, J. L., Ph.D. Thesis, Harvard University, Cambridge, Mass., 1967.
9. Gioumoussis, G., and Stevenson, D. P., *J. Chem. Phys.*, Vol. 29, p. 294, 1958.
10. Klein, F. S., and Friedman, L., *J. Chem. Phys.*, Vol. 41, p. 1789, 1964.
11. Friedman, L., *J. Chem. Phys.*, Vol. 41, Chapt. 7, 1964.
12. Chupka, W. A., Russell, M. E., and Refaey, K., *J. Chem. Phys.*, Vol. 48, p. 1518, 1968.

C. Compressional Waves in the Solar Wind,

T. W. J. Unti

The search continues for a clear example of a magnetosonic wave. In the *Mariner V* magnetometer read-

ings there are several promising segments of data. These segments are being processed for computer analysis.

As an example, day 206 contains a 12-h run of field and plasma data, during which the average field, bulk velocity, and average density remain almost constant. The amplitude of the field fluctuation is about one third the amplitude of the average field, with corresponding reasonably small amplitudes in the velocity and density fluctuations. This data sector will be divided into 12 1-h segments, and each segment will be analyzed independently.

If a linearly polarized longitudinal wave is present, the field will oscillate primarily in a single direction. Each 1-h subset, therefore, is examined for its line of oscillation. Consecutive data segments that are found to have the same, or nearly the same, line of oscillation are combined into a single data set. It is hoped that several subsets will coalesce in this manner. Such an extension of data sets may be indicative of wavelike phenomena.

But if the oscillations actually represent a compressional wave, the magnetic field and plasma must obey interrelations imposed by the hydromagnetic equations. If the magnetic field is given, the wave velocity of the particles is already determined by the equations. This suggests the following test: The magnetic field data are used, with the hydromagnetic equations, to predict the velocity fluctuations for a sonic wave. The curve obtained is then compared to the actual velocity measurements. If the curves agree, it may be concluded that sonic waves are present.

This will constitute the main test for magnetosonic waves, but a second test can be applied for verification. The density fluctuations are also determined by the field, through the hydromagnetic equations. Again, the computed density will be compared to the actual density measurements.

Various difficulties prevent a straightforward solution to the problem. In order to calculate the sonic wave velocity, the specific heat ratio and the electron temperature must be known. These quantities are not measured directly and must be inferred from the available information, perhaps by a least-squares technique relating all the wave parameters by means of the hydromagnetic equations. Also, it has been theoretically demonstrated by Barnes that, in contrast to Alfvén waves,

sonic waves damp very quickly. Therefore, all the quasi-periodic structures evident in the *Mariner V* data may be Alfvén waves and/or other phenomena.

D. Debever Vectors in Dyadic Notation,

B. K. Harrison⁴

One way to express the Petrov algebraic classification of the Weyl curvature tensor in differential geometry is to use the concept of *Debever vectors*. A Debever vector is a real null vector which satisfies a certain equation with the Weyl tensor. For the most general Weyl tensor (Petrov Type I), there are four distinct Debever vectors. If two or more Debever vectors are parallel (degenerate), the Weyl tensor is said to be degenerate, or of an algebraically special type.

Table 2 (Ref. 1) shows the different types of Petrov classification, the number of independent Debever vectors, and the equation satisfied by the degenerate Debever vectors. The bracket in the second column shows the number of degenerate vectors along with the number of nondegenerate vectors; [211], for example, means that there are two parallel vectors, which are thus degenerate, with two others not parallel to the first vectors or to each other. The degenerate vectors for a given type satisfy the equation for that type; the others satisfy the general equation (that for Type I). Brackets on indices represent antisymmetrization.

Table 2. Classification of Weyl tensor

Petrov type	Arrangement of vectors	Equations satisfied by Debever vectors
I	[1111]	$k_{[a}C_{b]cd[e}k_{f]}k^ck^d = 0$
II	[211]	$C_{bcd[e}k_{f]}k^ck^d = 0$
D	[22]	$C_{bcd[e}k_{f]}k^ck^d = 0$
III	[31]	$C_{bcd[e}k_{f]}k^ck^d = 0$
N	[4]	$C_{bcde}k^e = 0$
O	—	$C_{bcde} = 0$

For purposes of analysis, it is desirable to represent Debever vectors and their equations in the dyadic formulation of Wahlquist and Estabrook (Ref. 2). We use the following notation. The null vectors k_μ will be written $k_\mu = (1, \mathbf{u})$, where \mathbf{u} is a real unit 3-vector. (Since k_μ is real and null, its time component is nonzero and can be taken as unity.) The Weyl tensor is written in terms of components with respect to a local orthonormal frame,

and the components are written in the form of dyadics **A** and **B** (Ref. 2):

$$A_{ab} = C_{oao b} = -\frac{1}{4} \epsilon_{acd} \epsilon_{bfg} C^{cd fg} \quad (1)$$

$$B_{ab} = \frac{1}{2} \epsilon_{bcd} C_{oacd} \quad (2)$$

We also define a complex dyadic $\mathbf{C} = \mathbf{A} + i\mathbf{B}$. Indices are raised and lowered for the component indices with the Minkowski metric tensor.

We now write the equations of Table 2 for the Debever vectors in dyadic form. We find that they can be expressed in terms of a single dyadic equation for **C** and **u** for each Petrov type. It is to be remembered that **u** is real, $\mathbf{u}^2 = 1$, and that **C** is traceless and symmetric.

Type I.

$$\begin{aligned} \mathbf{C} - (\mathbf{C} \cdot \mathbf{u})\mathbf{u} - \mathbf{u}(\mathbf{u} \cdot \mathbf{C}) + i\mathbf{C}\mathbf{X}\mathbf{u} - i\mathbf{u}(\mathbf{u} \cdot \mathbf{C}\mathbf{X}\mathbf{u}) \\ + \frac{1}{2} (\mathbf{u} \cdot \mathbf{C} \cdot \mathbf{u}) (\mathbf{I} + \mathbf{u}\mathbf{u} + i\mathbf{I}\mathbf{X}\mathbf{u}) = 0, \\ \mathbf{u}(\mathbf{u} \cdot \mathbf{C} \cdot \mathbf{u}) - \mathbf{u} \cdot \mathbf{C} - i\mathbf{u} \cdot \mathbf{C}\mathbf{X}\mathbf{u} \neq 0 \end{aligned} \quad (3)$$

There are four noncoincident solutions for **u** in general.

Type II.

$$\begin{aligned} \mathbf{C} - (\mathbf{C} \cdot \mathbf{u})\mathbf{u} + i\mathbf{C}\mathbf{X}\mathbf{u} \\ + \frac{1}{2} (\mathbf{u} \cdot \mathbf{C} \cdot \mathbf{u}) (\mathbf{I} - \mathbf{u}\mathbf{u} + i\mathbf{I}\mathbf{X}\mathbf{u}) = 0, \\ \mathbf{u} \cdot \mathbf{C} \cdot \mathbf{u} \neq 0 \end{aligned} \quad (4)$$

The single solution of this equation represents the pair of coincident Debever vectors. The other two Debever vectors satisfy Eq. (3).

Type D. The Debever vectors are coincident in pairs; each vector satisfies Eq. (4).

Type III.

$$\mathbf{C} - (\mathbf{C} \cdot \mathbf{u})\mathbf{u} + i\mathbf{C}\mathbf{X}\mathbf{u} = 0, \quad \mathbf{C} \cdot \mathbf{u} \neq 0 \quad (5)$$

⁴Resident research associate assigned to JPL.

The single solution of this equation represents the triplet of coincident Debever vectors. The other Debever vector satisfies Eq. (3).

Type N.

$$\mathbf{C} + i\mathbf{C} \mathbf{X} \mathbf{u} = 0, \quad \mathbf{C} \neq 0 \quad (6)$$

The solution of this equation gives the four coincident Debever vectors.

Type O.

$$\mathbf{C} = 0 \quad (7)$$

This is the conformally flat case.

If we now define a dyadic \mathbf{D} ,

$$\mathbf{D} = \mathbf{C} + \frac{1}{2} (\mathbf{u} \cdot \mathbf{C} \cdot \mathbf{u}) \mathbf{I} \quad (= \mathbf{D}^T) \quad (8)$$

we note

$$\mathbf{C} = \mathbf{D} - \frac{1}{3} (\text{Tr} \mathbf{D}) \mathbf{I} \quad (9)$$

and find Eq. (4) to yield

$$\mathbf{D} - (\mathbf{D} \cdot \mathbf{u}) \mathbf{u} + i\mathbf{D} \mathbf{X} \mathbf{u} = 0 \quad (10)$$

Instead of solving this equation for \mathbf{u} , let us find the possible form of \mathbf{D} . We write

$$\begin{aligned} \mathbf{D} = & -3\alpha \mathbf{u}\mathbf{u} + \xi \mathbf{v}\mathbf{v} + \xi \mathbf{w}\mathbf{w} + \delta(\mathbf{u}\mathbf{v} + \mathbf{v}\mathbf{u}) \\ & + \epsilon(\mathbf{u}\mathbf{w} + \mathbf{w}\mathbf{u}) + \eta(\mathbf{v}\mathbf{w} + \mathbf{w}\mathbf{v}) \end{aligned} \quad (11)$$

where $(\mathbf{u}, \mathbf{v}, \mathbf{w})$ form a positive orthonormal triad. Equation (10) yields

$$\eta = \xi i, \quad \xi = -\xi, \quad \delta = -\epsilon i \quad (12)$$

Then if

$$\mathbf{y} = \frac{1}{(2)^{1/2}} (\mathbf{w} - i\mathbf{v}) \quad (13)$$

we find

$$\mathbf{D} = -3\alpha \mathbf{u}\mathbf{u} - 2\xi \mathbf{y}\mathbf{y} + \epsilon(2)^{1/2} (\mathbf{u}\mathbf{y} + \mathbf{y}\mathbf{u}) \quad (14)$$

and

$$\mathbf{u} = i\mathbf{y} \mathbf{X} \bar{\mathbf{y}} \quad (15)$$

(Bar denotes complex conjugate.)

We note that

$$\mathbf{y}^2 = 0, \mathbf{y} \cdot \bar{\mathbf{y}} = 1, \text{ and } \mathbf{u} \cdot \mathbf{y} = 0 \quad (16)$$

Then, with $\beta = -2\xi$, and $\gamma = \epsilon(2)^{1/2}$, we have from Eqs. (9) and (14)

$$\mathbf{C} = \alpha(1 - 3\mathbf{u}\mathbf{u}) + \beta \mathbf{y}\mathbf{y} + \gamma(\mathbf{u}\mathbf{y} + \mathbf{y}\mathbf{u}) \quad (17)$$

This is the general form \mathbf{C} must have to be algebraically special (i.e., not of Type I), with \mathbf{u} and \mathbf{y} satisfying Eqs. (15) and (16). Further restrictions, such as $\mathbf{u} \cdot \mathbf{C} \cdot \mathbf{u} = 0$, restrict \mathbf{C} to be more special than Type II.

If we note that

$$\mathbf{I} = \mathbf{y}\bar{\mathbf{y}} + \mathbf{y}\bar{\mathbf{y}}\mathbf{y} + \mathbf{u}\mathbf{u} \quad (18)$$

and define

$$\mathbf{z} = -\alpha \bar{\mathbf{y}} - \frac{1}{3} i\gamma \mathbf{y} \mathbf{X} \bar{\mathbf{y}} - \frac{1}{6} \beta \mathbf{y} \quad (19)$$

we can write \mathbf{C} in Eq. (17) in the form

$$\mathbf{C} = -3\mathbf{y}\mathbf{z} - 3\mathbf{z}\mathbf{y} + 2(\mathbf{y} \cdot \mathbf{z}) \mathbf{I} \quad (20)$$

This is the form obtained by Wahlquist⁵ from a consideration of the Cayley-Hamilton equation for \mathbf{C} .

By analysis of the two forms for \mathbf{C} , Eqs. (17) and (20), we now construct Table 3, summarizing the conditions

⁵Unpublished notes on algebraic classifications of the Weyl tensor dyadic, 1967.

Table 3. Conditions for \mathbf{C} to be a given Petrov type

Petrov type	Conditions for Eq. (17)	Conditions for Eq. (20)
II	$\alpha \neq 0, \gamma^2 \neq -3\alpha\beta$	$\mathbf{y} \cdot \mathbf{z} \neq 0, \mathbf{z}^2 \neq 0$
D	$\alpha \neq 0, \gamma^2 = -3\alpha\beta$	$\mathbf{y} \cdot \mathbf{z} \neq 0, \mathbf{z}^2 = 0$
III	$\alpha = 0, \gamma \neq 0$	$\mathbf{y} \cdot \mathbf{z} = 0, \mathbf{z}^2 \neq 0$
N	$\alpha = \gamma = 0, \beta \neq 0$	$\mathbf{y} \cdot \mathbf{z} = 0, \mathbf{z}^2 = 0, \mathbf{z} \neq 0$
O	$\alpha = \gamma = \beta = 0$	$\mathbf{z} = 0$

for \mathbf{C} to be each of the special types. The conditions for Eq. (20) have been given by Wahlquist;² those for Eq. (17) are obtained by substituting Eq. (17) into Eqs. (3)–(6), or by consideration of the related inequalities, and by noting that \mathbf{z} must satisfy $\mathbf{z}^2 = 0$ for Type D.

We note in Types II, III, and N, in which there is one degenerate Debever vector, that it is given by Eq. (15), $\mathbf{u} = i\mathbf{y} \times \bar{\mathbf{y}}$. In Type D, in which there are two degenerate Debever vectors, we can write

$$\mathbf{z} = k\mathbf{w} \quad (21)$$

where $\bar{\mathbf{w}} \cdot \mathbf{w} = 1$, and $\mathbf{w}^2 = 0$.

Then the second Debever vector can be shown to be

$$\mathbf{t} = i\mathbf{w} \times \bar{\mathbf{w}} \quad (22)$$

where \mathbf{w} may be expressed in terms of \mathbf{y} and \mathbf{u} :

$$\mathbf{w} = -\mathbf{y} \cos^2 \theta + \bar{\mathbf{y}} \sin^2 \theta + \mathbf{u}(2)^{1/2} \sin \theta \cos \theta, \quad 0 < \theta \leq \frac{\pi}{2} \quad (23)$$

where θ is a real parameter.

We then find, from Eqs. (22) and (23), that

$$\mathbf{t} = \frac{(2)^{1/2}}{2} \sin 2\theta (\mathbf{y} + \bar{\mathbf{y}}) + \mathbf{u} \cos 2\theta \quad (24)$$

Note that, if $\theta = \pi/2$, $\mathbf{t} = -\mathbf{u}$, but $\mathbf{w} \cdot \mathbf{y} = 1 \neq 0$, the space parts of the two Debever vectors may be antiparallel in Type D. We also note, with Wahlquist (Footnote 5), that an alternative form for \mathbf{C} in Type D is

$$\mathbf{C} = \sigma \left(\mathbf{I} - \frac{3\mathbf{s}\mathbf{s}}{\mathbf{s}^2} \right) \quad (25)$$

where \mathbf{s} is complex.

It is easily shown from Eqs. (20)–(24) that

$$\sigma = -k\mathbf{y} \cdot \mathbf{w} = -k \sin^2 \theta \quad (26)$$

and

$$\begin{aligned} \mathbf{s} &= \pm m \frac{i\mathbf{y} \times \mathbf{w}}{\mathbf{y} \cdot \mathbf{w}} \\ &= \pm m(\mathbf{u} - (2)^{1/2} \cot \theta \mathbf{y}) \end{aligned} \quad (27)$$

where $m = (\mathbf{s}^2)^{1/2}$. If $n = (\mathbf{s} \cdot \bar{\mathbf{s}})^{1/2}$ and $\mu = \pm 1$, then

$$\begin{Bmatrix} \mathbf{u} \\ \mathbf{t} \end{Bmatrix} = \frac{1}{n^2 + m\bar{m}} [\mu(\bar{m}\mathbf{s} + m\bar{\mathbf{s}}) + i\mathbf{s} \times \bar{\mathbf{s}}] \quad (28)$$

where $\mu = 1$ gives \mathbf{u} and $\mu = -1$ gives \mathbf{t} .

References

1. Pirani, F. A. E., *Introduction to Gravitational Radiation Theory*, (1964 Brandeis Lecture Notes), p. 321. Prentice-Hall, Inc., New York, 1965.
2. Wahlquist, H. D., and Estabrook, F. B., *Rigid Motions in Einstein Spaces*, Technical Report 32-868, p. 31. Jet Propulsion Laboratory, Pasadena, Calif., Mar. 15, 1966.

E. Dielectric Function of a Low-Density Electron Gas, J. S. Zmuidzinas⁶

Considerable insight into the physical properties of a metal can be obtained by studying a simple model of the metal consisting of a cold electron gas in a uniform neutralizing background of ions. The behavior of this idealized system is conveniently described by the dielectric function $\epsilon(\mathbf{k}, \omega)$ which measures the response of the system to a weak external electric field of frequency ω .

The dielectric function in the random-phase approximation (RPA) is given as (Ref. 1)

$$\epsilon_{RPA}(\mathbf{k}, \omega) = 1 - \frac{4\pi e^2}{\hbar k^2 V} \chi^0(\mathbf{k}, \omega) \quad (1)$$

where e is the electronic charge, V is the volume occupied by the electron gas, and the density-density response function χ^0 , in this approximation, is

$$\chi^0(\mathbf{k}, \omega) = \sum_{\mathbf{q}\sigma} \frac{n_{\mathbf{q}\sigma}^0 - n_{\mathbf{q}+\mathbf{k}\sigma}^0}{\omega - \omega_{\mathbf{q}\mathbf{k}}^0 + i\eta}, \quad \eta \rightarrow 0^+ \quad (2)$$

with

$$\omega_{\mathbf{q}\mathbf{k}}^0 = \frac{\hbar}{2m} [(\mathbf{q} + \mathbf{k})^2 - \mathbf{q}^2]$$

where m is the electron mass.

⁶The author wishes to acknowledge fruitful discussions with Dr. M. M. Saffren.

The zero-temperature Fermi distribution functions n^0 arise in Eq. (2) from linearizing the equations of motion for the particle-hole operators about the ground state of a non-interacting Fermi gas; for both spin orientations σ , one has

$$n_{k\sigma} = \begin{cases} 1, & \text{if } |k| < k_F \\ 0, & \text{if } |k| > k_F \end{cases}$$

where

$$k_F = (3\pi^2 n)^{1/3}$$

is the Fermi wavenumber, and n is the electron density. As is well known, the RPA expression (Eq. 1) for the dielectric function is valid only in the high-density limit (n large or $r_s = e^2 mn^{-1/3} \hbar^{-2} \ll 1$). Unfortunately, this limit is not representative of the actual metallic densities ($2 \lesssim r_s \lesssim 6$). Calculations of ϵ in the latter density regime are much more difficult, since the kinetic and the potential energies are comparable there, and neither can be treated as small in the first approximation. In the low-density regime ($r_s \gg 1$), matters are again simpler, since here the Coulomb energy dominates, and hence the strong-coupling methods are appropriate.

According to Wigner (Ref. 2), the electron gas solidifies into a lattice in the low-density limit. While this limit, too, is not representative of the actual metals, its study nevertheless is likely to be profitable, since it may throw some light on the poorly understood lattice-gas transition which is thought to occur at $r_s \sim 4$ (Ref. 3 and SPS 37-28, Vol. IV, pp. 132-134) as the electron density is increased from $r_s \gg 1$. In this article, we determine the RPA dielectric function in the low-density limit (LDL).

The simplest way of calculating ϵ in LDL is to linearize the particle-hole equations of motion not about the Fermi ground state but about the state of the electron lattice. Mathematically, this amounts to replacing n^0 in Eq. (2) by a distribution function appropriate to the electron lattice, determined as follows.

Let $|\Omega\rangle$ be the ground state of the electron lattice:

$$|\Omega\rangle = \mathcal{N} \left[\prod_{i\sigma} \psi_\sigma(x_i)^\dagger \right] |0\rangle$$

Here \mathcal{N} is a normalization constant, adjusted to make $\langle \Omega | \Omega \rangle = 1$; the product on i runs over all lattice sites

($N/2$ in number for each spin) in some fixed order; $\psi_\sigma(x_i)^\dagger$ are electron creation operators; and $|0\rangle$ is the electron vacuum. The state $|\Omega\rangle$ is an exact eigenstate of the interaction Hamiltonian and has the lowest possible eigenvalue if the electrons form a body-centered lattice (Ref. 2). However, the expectation value of the kinetic energy is infinite in this state. To avoid this infinity, one may "smear out" the lattice by making the substitution

$$\psi(x_i) \rightarrow \tilde{\psi}(x_i) = \int d^3x f(x - x_i) \psi(x_i)$$

where

$$f(x) = (\pi^{1/2} \ell)^{-3} \exp\left(\frac{-x^2}{\ell^2}\right)$$

and ℓ is taken much smaller than the lattice spacing $r_0 = n^{-1/3}$. The distribution function is defined as

$$n_{k\sigma} = V^{-1} \int d^3x \int d^3y \exp i\mathbf{k} \cdot (\mathbf{x} - \mathbf{y}) \langle \Omega | \psi_\sigma(\mathbf{x})^\dagger \psi_\sigma(\mathbf{y}) | \Omega \rangle$$

Using the approximation $\ell \ll r_0$, we find

$$\langle \Omega | \psi_\sigma(\mathbf{x})^\dagger \psi_\sigma(\mathbf{y}) | \Omega \rangle \simeq [(2\pi)^{1/2} \ell]^3 \sum_i f(\mathbf{x} - \mathbf{x}_i) f(\mathbf{y} - \mathbf{x}_i)$$

and hence

$$n_{k\sigma} = \frac{1}{2} n [(2\pi)^{1/2} \ell]^3 \exp\left(\frac{-k^2 \ell^2}{2}\right) \quad (3)$$

The distribution function Eq. (3) is Maxwellian with "temperature" T determined by $\ell^2 k^2 / 2 = m v^2 / 2 \kappa T$:

$$T = \hbar^2 / m \kappa \ell^2$$

where κ is the Boltzmann constant. Physically, T measures the kinetic energy which an electron acquires by virtue of its localization in a volume $\sim \ell^3$ centered about its lattice site.

Using Eq. (3) in Eq. (2), we find the following expression for the dielectric function in the LDL:

$$\epsilon_{LDL}(k, \omega) = 1 - \omega_p^2 \frac{m^2 \ell}{2^{1/2} \hbar^2 k^3} [Z(x_+) - Z(x_-)] \quad (4)$$

where

$$\omega_p = (4\pi n e^2 / m)^{1/2}$$

is the electron plasma frequency,

$$x_{\pm} = \frac{\ell}{2^{1/2} k} \left(\frac{m\omega}{\hbar} \pm \frac{1}{2} k^2 + i\eta \right)$$

and Z is the plasma dispersion function (Ref. 4)

$$Z(\xi) = \pi^{-1/2} \int_{-\infty}^{\infty} \frac{\exp(-x^2) dx}{x - \xi}$$

In the long-wavelength limit, Eq. (4) reduces to

$$\epsilon_{LDL|k \rightarrow 0} = 1 - \frac{\omega_p^2}{\omega^2} \left(1 + 3 \frac{k^2}{k_T^2} \right) + O(k^4) \quad (5)$$

where

$$k_T = \frac{m\ell\omega}{\hbar} \quad (6)$$

Equation (5) shows that the electron gas supports collective oscillations at the plasma frequency ω_p . Following Saffren's arguments (SPS 37-28, Vol. IV), one may regard the lattice electrons as moving in a harmonic-oscillator potential

$$V = \frac{e^2 x^2}{2R^3} = \frac{m\Omega^2 r^2}{2}$$

Where $R = r_s a_0$ and $a_0 = \hbar^2 / m e^2$ is the Bohr radius. One can then write ℓ^2 in $f(\underline{x})$ as

$$\ell^2 = \frac{2\hbar}{m\Omega} = 2r_s^{3/2} a_0^2$$

Substitution of this expression into Eq. (6) gives

$$k_T^2 = 8\pi r_s^{-3/2} a_0^{-2}$$

The high-density RPA expression for ϵ in the long-wave limit is (Ref. 5)

$$\epsilon_{RPA|k \rightarrow 0} = 1 - \frac{\omega_p^2}{\omega^2} \left(1 + \frac{9}{5} \frac{k^2}{k_{FT}^2} \right) + O(k^4) \quad (7)$$

where

$$\begin{aligned} k_{FT}^2 &= 4\pi^{-1} a_0^{-1} k_F \\ &= 4\pi^{-1} (3\pi^2)^{1/3} r_s^{-1} a_0^{-2} \end{aligned} \quad (8)$$

It is easy to verify that Eqs. (5) and (7) agree to order k^2 only when

$$r_s = \left[\frac{6\pi^2}{5(3\pi)^{1/3}} \right]^2 \simeq 16$$

Thus, in general, the high- and low-density random-phase approximations to $\epsilon(k \rightarrow 0)$ are different, and hence care must be exercised when performing extrapolations of these approximations away from their respective regions of validity.

References

1. Pines, D., and Nozières, P., *The Theory of Quantum Liquids*, Vol. I, pp. 281 and 283. W. A. Benjamin, Inc., New York, 1966.
2. Wigner, E., *Trans. Faraday Soc.*, Vol. 34, p. 678, 1938.
3. Carr, Jr., W. J., *Phys. Rev.*, Vol. 122, p. 1437, 1961.
4. Fried, B. D., and Conte, S. D., *The Plasma Dispersion Function*. Academic Press, New York, 1961.
5. Hubbard, J., *Phys. Lett.*, Vol. 25A, p. 709, 1967.

F. The Microwave Spectrum of the OD Free Radical, R. L. Poynter

1. Introduction

A few free radicals have been studied by microwave spectroscopic methods since the pioneering work on OH of Dousmanis, Sanders, and Townes (Ref. 1) in 1955. In particular, Powell and Lide⁷ (Ref. 2) have studied SO, CF₂, and Powell and Johnson⁸ have studied ClO. The OH and OD radicals are still of considerable interest, however, since they are amenable to an accurate theoretical analysis and their absorption frequencies are of importance to radio astronomy. Attempts to observe the low microwave frequency transitions by radio astronomy have been successful, but only after the characteristic transitions have been precisely located and identified in

⁷Powell, F. X., and Lide, Jr., D. R., "Microwave Spectrum of the CF₂ Radical," *J. Chem. Phys.* (in press).

⁸Powell, F. X., and Johnson, D., "The Microwave Spectrum of the ClO Radical," *J. Mol. Spectrosc.* (in press).

the laboratory (Refs. 3-5 and SPS 37-47, Vol. II, pp. 200-207). Radio astronomers have been reluctant to conduct searches over the radio spectrum based only on predictions computed from the early microwave OH and OD studies due to the length of time required to tune the narrow-band maser receivers which are used in radio astronomy.

We have found that the OH and OD radical frequencies can be accurately predicted from our new data. We have reported an analysis of the OH spectrum (SPS 37-47, Vol. III) in which we were able to make very good predictions of the astronomically interesting transitions at low microwave frequencies. In this article, we present a similar analysis of the OD spectrum in which we have been able to accurately predict and observe six new $\Delta F = 0$ transitions belonging to the OD radical.

At this time, we have not been able to observe any of the much weaker $\Delta F = \pm 1$ transitions, and, therefore, three out of the four hyperfine coupling constants remain undetermined. Although this severely limits our ability to predict the frequencies of any of the $\Delta F = \pm 1$ hyperfine transitions, it in no way affects our results for the $\Delta F = 0$ hyperfine transitions.

2. Experimental Techniques

The microwave spectrometer and absorption cell employed in this work were briefly described in SPS 37-51, Vol. III, pp. 193-197, and further details will be described in a later article. Here, we only point out a few changes that have been made.

The OD free radicals were generated by the fast chemical reaction of deuterium atoms with NO_2 . The deuterium atoms were generated by an electrodeless discharge in gaseous D_2 , which was mixed with a trace amount of either O_2 or NO_2 as a controlled impurity gas. The impurity was added to enhance the number of deuterium atoms produced by the discharge.

The spectrometer consists of the usual klystron oscillator for the microwave signal source, an absorption cell, a crystal detector which is used to drive a 100-kHz narrow-band amplifier, and a phase-sensitive detector. The absorption cell consists of two parallel stainless steel plates which are separated by a nominal 0.5 cm. These plates are mounted inside a large vacuum chamber, where the reacting gases can be controlled by a suitable pumping and inlet manifold system.

Frequency measurements are made by a slightly different method than previously reported. A frequency synthesizer (500-MHz) was used in combination with a narrow-band, high-power, high-frequency amplifier to drive a crystal harmonic multiplier. The beat frequency signal of the microwave klystron output with one of the crystal multiplier harmonics was detected by a fixed-tuned, narrow-band, crystal-controlled receiver. This method is very rapid and sufficiently accurate to give overall absorption frequency measurements to within ± 0.01 MHz at a microwave frequency of 38 GHz. However, the actual limitation to absorption measurement accuracies arises from the line widths, which are about 0.20 MHz. Greater accuracies could be obtained, but they are not required in the present application.

3. Energy Levels and Frequencies

The basic Hamiltonian given by Van Vleck (Ref. 6) and Frosch and Foley (Ref. 7) was used to calculate the molecular energy levels. Two centrifugal distortion terms were also included in the Hamiltonian to account for the observed spectrum (SPS 37-51, Vol. III). The complete matrix for the lambda doubling in OD is identical in form to that employed for the analysis of OH, except for a change in the nuclear spin from $\frac{1}{2}$ to 1. A nuclear spin of 1 will also change the number of F energy levels from 2 to 3, precipitating a change in the computer logic details.

The complete Hamiltonian matrix is exactly diagonalized by a computer program, and the resulting energy levels are then employed to compute the molecular frequencies. The unitary transformation matrix used in the Hamiltonian diagonalization is retained and used to calculate the transition intensities. The accuracy of the results has been checked by writing a fourth-order perturbation-type computer program. Both programs converge to the same results. Further checks were employed by writing these programs in successive stages, with and without nuclear hyperfine interactions. The first-stage computation involved only the pure lambda doubling. These results were checked by comparing with the pure lambda doubling frequencies as derived from the experimental results. When the proper convergence was obtained, the nuclear hyperfine splitting terms were added. These results were checked directly against the observed spectra.

To analyze the observed frequencies, it is necessary to change the molecular parameters, compute a predicted spectrum, and compare the predictions with experimental observations. Corrections to the initial parameters

are computed from the differences between the observed and predicted spectra. This is essentially an iterative process, which is best handled by employing least-squares methods. Thus, the energy level/frequency program was compressed to bare essentials and merged with a standard least-squares program.

The combination of these programs permitted a rapid evaluation of our experimental data. It was possible to show whether or not various theoretical terms were important in explaining the observed spectrum.

The least-squares-computed spectral parameters could be used in the full program to predict all of the absorption lines which would fall in the microwave region accessible to our spectrometer. We also computed the expected laboratory intensities, to determine whether or not we could reasonably expect to see any of the predicted lines. Further details of the analytical and computational results will be reported later.

4. Results

We assumed the same optical spectral constants which DST used. The validity of this assumption will be examined later. We then calculated approximate values for the remaining lambda doubling parameters from the results of Dousmanis, Sanders, and Townes. All parameters were then inserted into the least-squares program, along with the prior-observed frequencies. This process resulted in a "refined" set of molecular parameters. It also showed that three of the molecular constants were very insensitive parameters in fitting the lambda doubling spectrum. These constants were (1) the energy difference between the Σ and the π electronic states, (2) the rotational constant for the Σ state, B_Σ , and (3) either (but *not* both) the rotational constant for the π state *or* the spin-orbit coupling constant, A . These three constants were held fixed at the values obtained from optical spectroscopic results. On this basis, it was possible to obtain a fair fit of the spectrum. This fit also showed that a number of the observed frequencies reported by Dousmanis, Sanders, and Townes were in error. This forced us to remeasure all of the frequencies that had been reported, since there was no simple way of determining which of those frequencies were incorrect.

In this process, we were able to resolve all of the $^2\pi_{3/2}$ transitions into the expected triplets for the first time. We were thus able to obtain a very precise value for the d nuclear hyperfine coupling constant. In addition, we could now predict all of the expected microwave transi-

tions which would fall below 40 GHz. Six predicted lines were accessible to measurement with our spectrometer. They were observed very close to their predicted locations. The complete set of absorption lines is presented in Table 4. This set of lines (30) was then used to compute a "final" set of molecular constants which are presented in Table 5. The quality of the derived constants can be judged from the extremely close agreement obtained between the calculated and observed frequencies. If the agreement were to a nominal 0.5 MHz, it would be a good fit by microwave spectroscopic standards. The

Table 4. Comparison of calculated and observed OD transitions

Assignment		Frequency, MHz		Frequency difference (observed - calculated), MHz
J	F → F'	Calculated	Observed	
² π _{1/2} electronic state				
5/2	3/2	8110.740	8110.72	-0.020
	5/2	8117.999	8117.99	-0.009
	7/2	8128.160	8128.13	-0.030
7/2	5/2	9578.933	9578.90	-0.033
	7/2	9586.279	9586.32	+0.041
	9/2	9595.723	9595.74	+0.017
9/2	7/2	10192.22	10192.21	-0.011
	9/2	10199.53	10199.56	+0.029
	11/2	10208.47	10208.50	+0.035
11/2	9/2	9914.722	9914.70	-0.022
	11/2	9921.936	9921.95	+0.014
	13/2	9930.462	9930.44	-0.022
² π _{3/2} electronic state				
11/2	9/2	8671.548	8671.60	+0.052
	11/2	8672.409	8672.37	-0.039
	13/2	8673.426	8673.35	-0.076
13/2	11/2	12917.03	12917.08	+0.051
	13/2	12918.10	12918.13	+0.026
	15/2	12919.34	12919.33	-0.014
15/2	13/2	18009.39	18009.46	+0.073
	15/2	18010.66	18010.63	-0.034
	17/2	18012.11	18012.13	+0.017
17/2	15/2	23907.01	23907.08	+0.068
	17/2	23908.46	23908.44	-0.039
	19/2	23910.12	23910.04	-0.080
19/2	17/2	30565.34	30565.42	+0.083
	19/2	30566.98	30566.95	-0.029
	21/2	30568.79	30568.72	-0.074
21/2	19/2	37940.59	37940.58	-0.012
	21/2	37942.39	37942.43	+0.037
	23/2	37944.37	37944.36	-0.006

constants of Table 5 give an agreement of almost 5 to 10 times better than this, which is an excellent fit! It should also be pointed out that the same centrifugal distortion effects, D and δ , that occur in OH must also be used here to compute the results shown in Table 4.

The very close fit between the computed and observed spectral lines gives confidence that other microwave

absorption lines can be reliably predicted. A complete list of the $\Delta F = 0$ lines which may be of interest for radio astronomy is given in Table 6. The $\Delta F = \pm 1$ lines have been omitted because there is insufficient experimental data available to determine the three nuclear hyperfine coupling constants, a , b , and c , which are required to predict the line frequencies. These constants have no effect upon the $\Delta F = 0$ transitions.

Table 5. Least-squares-evaluated molecular constants for the OD molecule

Constant	MHz
E_{σ}^a	9.797981×10^5
B_{σ}^a	2.70713×10^5
B_{π}^a	2.95836×10^5
$A_{\text{spin-orbit}}$	$-4.16227 \times 10^6 \pm 0.000151^b$
$\langle \Sigma BL_y \pi \rangle$	$2.005746 \times 10^5 \pm 0.000037^b$
$\langle \Sigma (2B + A)L_y \pi \rangle$	$-1.890918 \times 10^6 \pm 0.000038^b$
$D_{\text{centrifugal-distortion}}$	30.096 ± 0.018^b
δ	-2.865 ± 0.028^b
λ^c	-14.0693 ± 0.024^b
$d_{\text{hyperfine}}$	8.747 ± 0.017^b

*These constants are obtained from the optical spectroscopic constants that DST used, under the assumption that they picked the best values.
b"Error limits" quoted are the standard deviation. No "scale" factors have been used as yet.
c λ accuracy is determined by uncertainty in B_{π} .

References

1. Dousmanis, G. C., Sanders, Jr., T. M., and Townes, C. H., "Microwave Spectra of the Free Radicals OH and OD," *Phys. Rev.*, Vol. 100, p. 1735, 1955.
2. Powell, F. X., and Lide, Jr., D. R., "Microwave Spectrum of the SO Radical," *J. Chem. Phys.*, Vol. 4, p. 1413, 1964.
3. Ehrenstein, G., Townes, C. H., and Stevenson, M. J., "Ground State A-Doubling Transitions of OH Radical," *Phys. Rev. Lett.*, Vol. 3, p. 40, 1959.
4. Weinreb, S., Barrett, A. H., Meeks, M. L., and Henry, J. C., "Radio Observations of OH in the Interstellar Medium," *Nature*, Vol. 200, p. 829, 1963.
5. Zuckerman, B., Palmer, P., Penfield, H., and Lilley, A. E., "Detection of Microwave Radiation from the $^2\pi_{1/2}$, $J = 1/2$ State of OH," *J. App. Phys.*, Vol. 153, p. L69, 1968.
6. Van Vleck, J. H., *Phys. Rev.*, Vol. 33, p. 467, 1929.
7. Frosch, R. A., and Foley, H. M., *Phys. Rev.*, Vol. 88, p. 1337, 1952.

Table 6. OD lambda doubling transitions ($\Delta F = 0$)

J	F(I)	F(F)	Frequency, MHz	A(F, FP), s ⁻¹	Intensity, cm ⁻¹	J	F(I)	F(F)	Frequency, MHz	A(F, FP), s ⁻¹	Intensity, cm ⁻¹
² $\pi_{1/2}$ electronic state						² $\pi_{1/2}$ electronic state					
0.5	0.5	0.5	3093.647	3.17×10^{-10}	2.81×10^{-6}	1.5	0.5	0.5	310.143	5.66×10^{-11}	9.41×10^{-9}
0.5	1.5	1.5	3111.141	3.22×10^{-10}	2.86×10^{-6}	1.5	1.5	1.5	310.232	5.66×10^{-11}	9.42×10^{-9}
1.5	0.5	0.5	5887.786	4.56×10^{-10}	3.49×10^{-6}	1.5	2.5	2.5	310.381	5.67×10^{-11}	9.43×10^{-9}
1.5	1.5	1.5	5894.695	4.58×10^{-10}	3.50×10^{-6}	2.5	1.5	1.5	1190.580	1.34×10^{-11}	1.79×10^{-7}
1.5	2.5	2.5	5906.210	4.61×10^{-10}	3.52×10^{-6}	2.5	2.5	2.5	1190.819	1.34×10^{-11}	1.79×10^{-7}
2.5	1.5	1.5	8110.742	5.46×10^{-10}	3.25×10^{-6}	2.5	3.5	3.5	1191.154	1.34×10^{-11}	1.79×10^{-7}
2.5	2.5	2.5	8118.001	5.48×10^{-10}	3.26×10^{-6}	3.5	2.5	2.5	2822.022	9.63×10^{-11}	9.40×10^{-7}
2.5	3.5	3.5	8128.162	5.50×10^{-10}	3.28×10^{-6}	3.5	3.5	3.5	2822.452	9.63×10^{-11}	9.40×10^{-7}
3.5	2.5	2.5	9578.938	5.41×10^{-10}	2.27×10^{-6}	3.5	4.5	4.5	2823.004	9.64×10^{-11}	9.41×10^{-7}
3.5	3.5	3.5	9586.283	5.42×10^{-10}	2.28×10^{-6}	4.5	3.5	3.5	5304.021	3.94×10^{-10}	2.57×10^{-6}
3.5	4.5	4.5	9595.727	5.44×10^{-10}	2.28×10^{-6}	4.5	4.5	4.5	5304.663	3.94×10^{-10}	2.58×10^{-6}
4.5	3.5	3.5	10192.229	4.51×10^{-10}	1.21×10^{-6}	4.5	5.5	5.5	5305.448	3.94×10^{-10}	2.58×10^{-6}
4.5	4.5	4.5	10199.539	4.52×10^{-10}	1.21×10^{-6}	5.5	4.5	4.5	8671.537	1.15×10^{-9}	4.61×10^{-6}
4.5	5.5	5.5	10208.473	4.53×10^{-10}	1.22×10^{-6}	5.5	5.5	5.5	8672.398	1.15×10^{-9}	4.61×10^{-6}
5.5	4.5	4.5	9914.733	3.12×10^{-10}	4.87×10^{-7}	5.5	6.5	6.5	8673.414	1.15×10^{-9}	4.61×10^{-6}
5.5	5.5	5.5	9921.946	3.13×10^{-10}	4.98×10^{-7}	6.5	5.5	5.5	12917.015	2.70×10^{-9}	6.05×10^{-6}
5.5	6.5	6.5	9930.472	3.14×10^{-10}	4.89×10^{-7}	6.5	6.5	6.5	12918.089	2.70×10^{-9}	6.05×10^{-6}
6.5	5.5	5.5	8753.001	1.70×10^{-10}	1.40×10^{-7}	6.5	7.5	7.5	12919.329	2.70×10^{-9}	6.05×10^{-6}
6.5	6.5	6.5	8760.091	1.71×10^{-10}	1.40×10^{-7}	7.5	6.5	6.5	18009.369	5.41×10^{-9}	6.21×10^{-6}
6.5	7.5	7.5	8768.271	1.71×10^{-10}	1.41×10^{-7}	7.5	7.5	7.5	18010.647	5.41×10^{-9}	6.21×10^{-6}
7.5	6.5	6.5	6737.080	6.38×10^{-11}	2.52×10^{-8}	7.5	8.5	8.5	18012.095	5.41×10^{-9}	6.21×10^{-6}
7.5	7.5	7.5	6744.035	6.40×10^{-11}	2.53×10^{-8}	8.5	7.5	7.5	23906.992	9.67×10^{-9}	5.21×10^{-6}
7.5	8.5	8.5	6751.917	6.42×10^{-11}	2.54×10^{-8}	8.5	8.5	8.5	23908.459	9.67×10^{-9}	5.21×10^{-6}
8.5	7.5	7.5	3907.517	1.05×10^{-11}	1.81×10^{-9}	8.5	9.5	9.5	23910.100	9.68×10^{-9}	5.21×10^{-6}
8.5	8.5	8.5	3914.336	1.05×10^{-11}	1.82×10^{-9}	9.5	8.5	8.5	30565.316	1.59×10^{-8}	3.67×10^{-6}
8.5	9.5	9.5	3921.957	1.06×10^{-11}	1.83×10^{-9}	9.5	9.5	9.5	30566.958	1.59×10^{-8}	3.67×10^{-6}
9.5	8.5	8.5	307.800	4.40×10^{-12}	3.04×10^{-12}	9.5	10.5	10.5	30568.772	1.59×10^{-8}	3.67×10^{-6}
9.5	9.5	9.5	314.489	4.69×10^{-12}	3.24×10^{-12}	10.5	9.5	9.5	37940.569	2.44×10^{-8}	2.21×10^{-6}
9.5	10.5	10.5	321.881	5.03×10^{-12}	3.47×10^{-12}	10.5	10.5	10.5	37942.371	2.44×10^{-8}	2.21×10^{-6}
10.5	9.5	9.5	4019.392	8.52×10^{-12}	2.15×10^{-10}	10.5	11.5	11.5	37944.344	2.44×10^{-8}	2.21×10^{-6}
10.5	10.5	10.5	4012.827	8.48×10^{-12}	2.14×10^{-10}						
10.5	11.5	11.5	4005.636	8.43×10^{-12}	2.13×10^{-10}						